University of Stuttgart
Germany

Validating Sentinel 3 altimetry over the Neckar River using GNSS Interferometric Reflectometry

Ziqing Yu

Master thesis

in the degree program
Geodesy and Geoinformatics

at the Institute of Geodesy
University of Stuttgart

Stuttgart, September 2023

Supervisor: Dr.-Ing. Mohammad Tourian
Prof. Dr. James Foster
Universität Stuttgart

GIS

Erklärung der Urheberschaft

Ich erkläre hiermit an Eides statt, dass ich die vorliegende Arbeit ohne Hilfe Dritter und ohne Benutzung anderer als der angegebenen Hilfsmittel angefertigt habe; die aus fremden Quellen direkt oder indirekt übernommenen Gedanken sind als solche kenntlich gemacht. Die Arbeit wurde bisher in gleicher oder ähnlicher Form in keiner anderen Prüfungsbehörde der Universität Stuttgart oder einer anderen Hochschule vorgelegt, und auch noch nicht veröffentlicht.

_____
Ort, Datum

_____
Unterschrift

Declaration of authorship

I declare in lieu of an oath, that the research reported within this thesis has been conducted by the author unless indicated otherwise. Ideas provided directly or indirectly by others have been marked for that. The material contained within this thesis has not previously been submitted for a degree to the examination authority of the University of Stuttgart or any other University, and is also not published otherwise.

Abstract

GNSS-IR is a technique that enables the constant observation of water surface height using reflected GNSS signals from water surface. It offers a simple monitoring approach compared to other techniques, requiring only a GNSS receiver near the water. The principle of the technique involves analyzing signal-to-noise data by converting signals from the time domain to the frequency domain.

Satellite altimetry is another powerful technique for long-term water monitoring, providing extensive spatial coverage. The retrieval of water level from altimetry waveforms, known as retracking, is susceptible to errors due to various factors, despite the development of multiple retracking algorithms for different waveform types.

The Sentinel-3 satellite mission, operated by ESA and EUMETSAT, is designed to monitor Earth's surface topography and climate while providing altimetry data. In this study, the altimetry results for the Neckar river from Sentinel-3 mission will be validated using the GNSS-IR technique. Due to the absence of a permanent GNSS receiver at the ideal measurement point, the measurement campaigns have a limited duration of a few hours each time. To better receive the reflected signals from water, GNSS antennas are rotated in the last 2 campaigns. To maximize the utilization of GNSS signal-to-noise ratio (SNR) data and capture the dynamic water level changes during observations, a novel technique is developed. This technique involves splitting the data according to time and multiplying the Lomb-Scargle Periodograms(LSP) from different satellites within specific time ranges. By extracting the peaks of the multiplied periodograms, a time series can be generated. The altimetry results from the Sentinel-3 mission will then be validated using this time series. To enhance the quality of GNSS-IR results, various methods have been implemented, including selecting different campaign locations, rotating GNSS receivers, and applying data filters such as elevation angle.

GNSS-IR is proved to be a able to monitor the inland small water body and rotating the GNSS antenna can improve the result quality. All seven retrackers from the Sentinel-3 mission are validated using water level data obtained from GNSS-IR. The altimetry water level is higher as the result from GNSS-IR and this offset varies for different retrackers from about 0.1 to 0.4 meters. In the challenging Neckar area with a narrow river width and complex environment, OCOG has demonstrated the best performance in terms of both availability and accuracy, the difference is from 0.03 to 0.17 meters in all experiments.

The source code for this work can be found in https://github.com/ziqing97/gnss_ir_analyze

Contents

Chapter 1

Introduction

1.1 Motivation

Water, as an essential element for sustaining life on Earth, plays a vital role in shaping natural landscapes, ecosystems, and human civilizations (Ashraf and Mohd Hanafiah, 2019), (Group et al., 2001). However, the impact of global warming and human activities on inland surface water has become increasingly evident, disrupting the delicate balance of the hydrological cycle. In recent decades, there has been a noticeable transformation in the characteristics of water bodies that were once considered permanent. This shift has been documented over the past three decades, indicating substantial changes in the state and behavior of these water systems (Pekel et al., 2016), (Lutz et al., 2014). As recent as summer 2021, record rainfall caused severe flooding events adjacent to the Rhine River in North Rhine-Westphalia and Rhineland-Palatinate, in which 40,000 lives were directly affected and several lost (Bosseler et al., 2021). These observations underscore the urgent need to comprehensively understand and address the evolving dynamics of water bodies in the face of environmental challenges.

The study of global water distribution is of paramount importance in understanding the complex interplay among hydrological processes, environmental sustainability, and human development (Wada et al., 2011). This interdisciplinary field of research delves into the dynamic fluctuations of water levels in rivers, lakes, and oceans, providing insights into the intricate interactions between these water bodies and their surrounding environments. By examining the patterns and variations in water distribution, researchers gain a deeper understanding of the fundamental processes that shape our planet's hydrological cycle and influence the availability of water resources(Davie, 2019). This knowledge serves as a foundation for effective water resource management, ecosystem preservation, and sustainable development practices worldwide. Indeed, monitoring water elevation, encompassing sea, lake, and river levels, is confronted with the vulnerabilities associated with anthropogenic climate change. This presents a considerable challenge in the field of water studies (Goudie, 2006). To address this challenge, several methods have been developed, including gauge and satellite-based techniques, to measure water levels effectively.

However, the use of gauges in the study suffers from certain limitations. The spatial distribution and number of gauges can undergo significant changes over time (Lorenz et al., 2014). Moreover, the availability and accessibility of in situ gauging stations are often restricted, particularly in many regions worldwide where these stations are not publicly accessible or adequately maintained by local authorities (Gleick, 2003). Satellite altimetry, on the other hand, offers global coverage of water bodies. However, it has its own limitations.

The technique does not provide continuous measurements, as the water level at a specific location can only be observed every 27 days using satellites such as Sentinel-3[1]. Additionally, satellite altimetry measures the range from the satellite ellipsoidal altitude and computes the water elevation by subtracting the range measurement (section 2.1). This process introduces additional errors into the final results.

Consequently, the development of alternative methods becomes imperative to accurately measure water levels in areas where in situ gauging stations are lacking. These alternative approaches play a crucial role in bridging the data gap and facilitating comprehensive water level monitoring, thereby supporting informed decision-making and sustainable water resource management. One such alternative method is the GNSS-IR (Global Navigation Satellite System-Interferometric Reflectometry) technique, which estimates environmental parameters near a geodetic-quality GNSS site by analyzing the signal-to-noise ratio (SNR) patterns created by the interference of direct and reflected GNSS signals (Roesler and Larson, 2018). A GNSS receiver can be easily and flexibly deployed near the water body, allowing for continuous observations. By analyzing the geometry and properties of multipath signals, it is possible to compute the height of the receiver over the water surface. Furthermore, by fixing the GNSS receiver in a specific location or utilizing high-resolution positioning techniques like Real-Time Kinematic (RTK) or Precise Point Positioning (PPP), the errors associated with the measurement can be significantly reduced.

GNSS-IR is a relatively new technology that holds considerable promise in terms of its reliability and potential. Its application in testing the reliability and assessing the uncertainty of this technique is an interesting area of research. Additionally, GNSS-IR offers a valuable opportunity to validate water level measurements obtained through satellite altimetry missions, particularly in areas where other data sources are limited or unavailable.

1.2 Objectives and Outline

The aim of this study is to measure the surface height of the Neckar River using GNSS-IR methods. Suggestions for the measurement will be summarized during the campaigns. Subsequently, the data will be processed using the multiplied Lomb-Scargle Periodogram to generate a GNSS-IR-based height timeseries with uncertainty, enabling the analysis of GNSS-IR data quality. Finally, a comparison will be made between the heights derived from GNSS-IR and the altimetry results obtained from different retrackers of the Sentinel-3 mission.

The study begins by introducing the two technologies utilized in this research. In chapter 3, an overview of the measurement area, the campaigns conducted, and the other data sources employed for the study is provided. chapter 4 elaborates on our periodogram multiplication method and the determination of ellipsoidal water levels using GNSS-IR. Next, in chapter 5, we present the results obtained from the GNSS-IR analysis and utilize them to assess satellite altimetry. chapter 6 summarizes our measurement experience, discusses the achieved results, and presents conclusions. Additionally, we provide an outlook on potential future work.

---

[1]https://sentinels.copernicus.eu/web/sentinel/missions/sentinel-3/satellite-description/orbit

Chapter 2

Monitoring Water Using Satellite Altimetry and GNSS-IR

2.1 Concepts to Satellite Altimetry

The principle behind satellite altimetry is straightforward: a radar pulse is transmitted from the satellite and reflected off the water surface, subsequently received by the satellite. By analyzing the waveform of the reflected pulse and measuring its travel time, the range can be calculated, incorporating various correction data. The water surface elevation, relative to the reference ellipsoid, can then be determined by subtracting the range from the satellite's altitude. This process is depicted in Figure 2.1. Furthermore, Figure 2.2 visually illustrates the different stages of interaction between the radar pulse and water surface, as well as the waveform generated from their interaction.
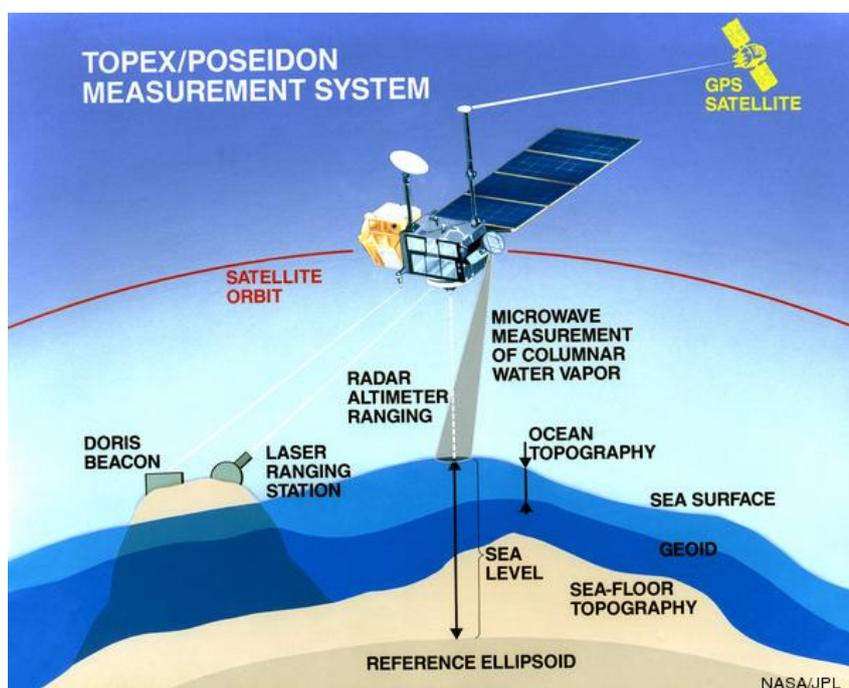

Figure 2.1: Visualization of the measurement principle of satellite altimetry mission TOPEX. (source: JPL)

During the initial stage of satellite altimetry, the radar pulse is transmitted from the satellite in the nadir direction, reaching the water surface as a point. Subsequently, the point evolves into a spherical shell, resulting in a significant increase in the returned power between times t_0 and t_1, referred to as the *leading edge*. Following this, the shell reaches its maximum area, transforming the wavefront into a filled circle that expands in size and thickness after time t_1. At this stage, the returned power gradually decreases, known as the *trailing edge* (Tourian, 2013). To ensure accurate altimetry measurements, it is crucial to precisely determine the middle time point on the leading edge, between t_0 and t_1, which is achieved through waveform retracking. However, waveforms over inland water bodies often exhibit noisy leading and trailing edges, making it challenging for the on-board tracker to identify the half-power point accurately. Consequently, these noisy edges can lead to inaccurate range measurements by the on-board tracker, resulting in erroneous data (Tourian, 2013).
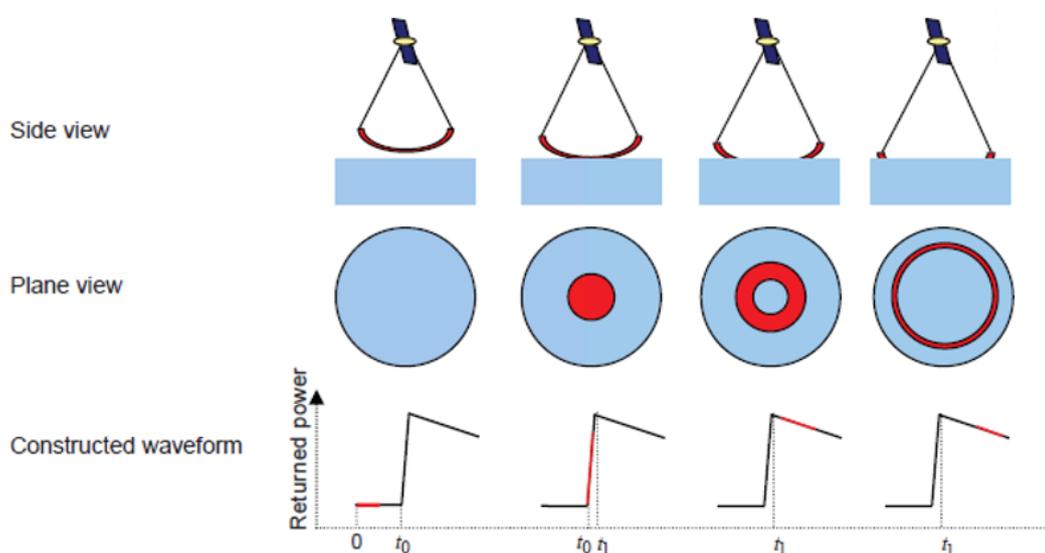

Figure 2.2: Interaction principle between radar pulse and surface (Tourian, 2013)

There are two modes for setting the tracking window in satellite altimetry. The closed-loop mode determines the tracking window in near-real time based on the analysis of the previously received waveform. On the other hand, the open-loop mode utilizes a-priori information in the form of pseudo-Digital Elevation Model (DEM) look-up tables. These look-up tables provide approximate elevation information for the satellite's instantaneous location on the Earth's surface (Robinson, 2004). In satellite altimetry, different retrackers employing physical and empirical approaches are utilized to process the widely varying shape and size of returned waveforms (Shu et al., 2020). These waveforms can be categorized into four classes:

- Fitting algorithm: β-parameter retracking (Martin et al., 1983).

- The off center of gravity technique (OCOG) (Wingham et al., 1986).

- Threshold retracking (Davis, 1993).

- Surface/volume scattering retracking (Ridley and Partington, 1988).

Each of them has its highest performance over a specific waveform shape (Deng and Featherstone, 2006).

2.2 Concepts to GNSS Interferometric Reflectometry

Global navigation satellite system (GNSS) including GPS from USA, GLONASS from Russia, Galileo from European Union and Beidou from China is developed to provide autonomous geopositioning. Ths satellites broadcast a signal that contains orbital data and the precise time the signal was transmitted. The receiver compares the time of broadcast in the transmission of at least 4 different satellites (giving the pseudorange) and these measurements are used to obtain its position and reception time. The accuracy of this measurement can be influenced by several factors, one major error source is from multipath.

Multipath refers to the phenomenon where one or more signals reach the GNSS antenna through indirect paths. When the multipath signal is reflected from a relatively smooth surface, it introduces errors in both pseudorange and carrier phase measurements, making it the primary error source in GNSS positioning (Braasch, 1996). However, multipath can also be utilized to determine physical parameters such as reflector distance and surface moisture (Bilich and Larson, 2007). Previous studies have proposed various methods to capture the orientation and reflectivity of objects within the GNSS multipath environment. For instance, Park et al. (2004) developed a directional antenna capable of measuring the orientation and magnitude of multipath effects. Each of these methods has its own advantages and disadvantages. Bilich and Larson (2007) presented a method where the multipath signal-to-noise ratio (SNR) can be extracted to evaluate the receiver height over the reflective surface.

2.2.1 First Fresnel Zone

As presented in Figure 2.3, When a GNSS signal encounters a smooth earth surface, it follows the shortest path to the GNSS receiving antenna when it reaches a point in the plane of incidence, where the angle of incidence equals the angle of reflection. Any other point on the surface results in a longer distance from the satellite to the receiver, leading to a greater phase shift in the correlation process compared to the signal reflecting at the specular point (Katzberg et al., 2006). GNSS satellites transmit signals with an aperture angle, resulting in the contribution of various areas on the reflector surface to the reflected signal (Zimmermann et al., 2019). If the surface remains flat over a distance of multiple wavelengths, the reflected signal appears to originate from an ellipse known as the first Fresnel Zone (FFZ). The size of this ellipse is determined by the wavelength of the signal (Larson and Nievinski, 2013).

2.2.2 Determination of Receiver Height with SNR

As shown in Figure 2.4, the GNSS receiver is located at point R on the z-axis, with the reflection point lying on the x-axis. The receiver height h corresponds to the z-coordinate of point R and
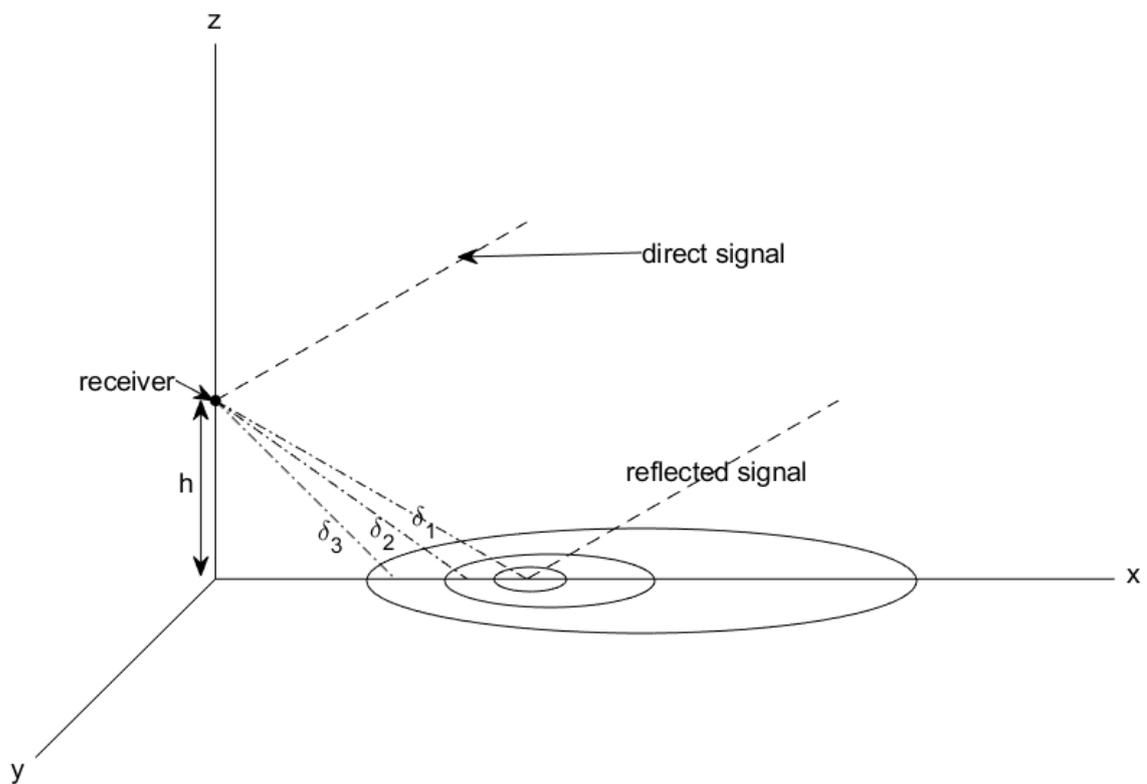
Figure 2.3: *The cross-correlation of the PRN code at different delays gives rise to the lambda-square profile, which is a function of range on the reflecting surface. The sensitivity profile corresponds to an elliptical area on the surface and extends one-half code chip at each delay bin*

ϵ is the elevation angle. Based on different ϵ, the relationship between h and multipath length. When ϵ is smaller than $45°$ (Figure 2.5), the multipath length δ is equal to $P'_r - P_i$. There is:

$$\frac{P'_r + P_i}{\cos(\epsilon)} = \frac{h}{\sin(\epsilon)} \cdot 2 \tag{2.1}$$

$$P'_r = \frac{h}{\sin(\epsilon)} \tag{2.2}$$

By combining 2 equations above we have $P_i = (2h\cos^2(\epsilon) - h)/\sin(\epsilon)$, and thus:

Figure 2.4: *Geometric view of direct and multi-path GNSS signals, where yellow line is the direct signal and green line is the reflected signal from water surface. ϵ is the elevation angle.*

$$\delta = P'_r - P_i = \frac{2h - 2h\cos^2(\epsilon)}{\sin(\epsilon)} \tag{2.3}$$

$$= \frac{2h\sin^2(\epsilon)}{\sin(\epsilon)} \tag{2.4}$$

$$= 2h\sin(\epsilon) \tag{2.5}$$

When ϵ is bigger than $45°$ (Figure 2.6), the delayed path length $P_i + P_r$ is equal to $P_i + P_{r'}$ since P_r and $P_{r'}$ are two waists of an isosceles triangle. Note that $P_i + P_{r'}$ is the longest side of the largest right-angled triangle, and the hypotenuse of this triangle has a length of $2h$. If we define $P_i + P_{r'}$ as δ, we can express the relationship between multipath length and receiver height simply as:

$$\delta = 2h\cos\left(\frac{\pi}{2} - \epsilon\right) = 2h\sin(\epsilon) \tag{2.6}$$

When $\epsilon = 45°$ (Figure 2.7), multipath length $\delta = P_r = h/\sin(\epsilon)$ and therefore:

$$\delta = \frac{h}{\frac{\sqrt{2}}{2}} \tag{2.7}$$

$$= \sqrt{2} \cdot h \tag{2.8}$$

$$= 2\sin(45°)h \tag{2.9}$$

Concluding all 3 cases discussed above, the relationship between δ and h can be written as:
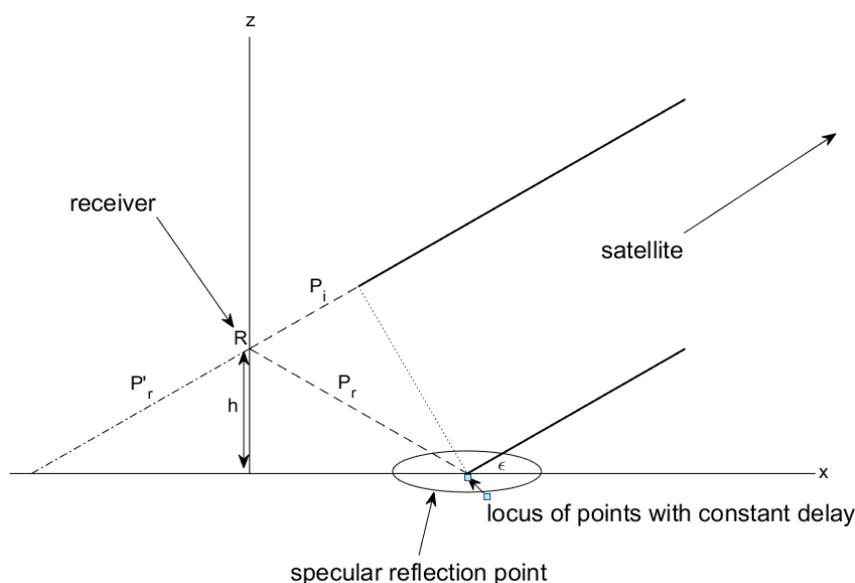$\delta = 2h\sin\epsilon$

Figure 2.5: *The geometric relationship between receiver height h and multipath length when elevation angle ϵ is small than 45°. Multipath length δ is equal to $P_i + P_r$, receiver R is on the z-axis.*

The signal-to-noise ratio (SNR) of the direct signal can be expressed as shown in Equation 2.10. In comparison, the signal power of the reflected signal is much weaker, and the phase is additionally delayed, resulting in the reflected signal being represented by Equation 2.11.

$$\text{SNR}_{dir} = V\cos(\varphi) \tag{2.10}$$

$$\text{SNR}_{ref} = \alpha \cdot V\cos(\varphi + \Delta\varphi) \tag{2.11}$$

This delayed phase can actually represent the length of the multi-path:

$$\Delta\varphi = \frac{2\pi}{\lambda}\delta \tag{2.12}$$

After combining the Equation 2.6 and Equation 2.12, we find the relationship between the antenna height and the reflected SNR data:

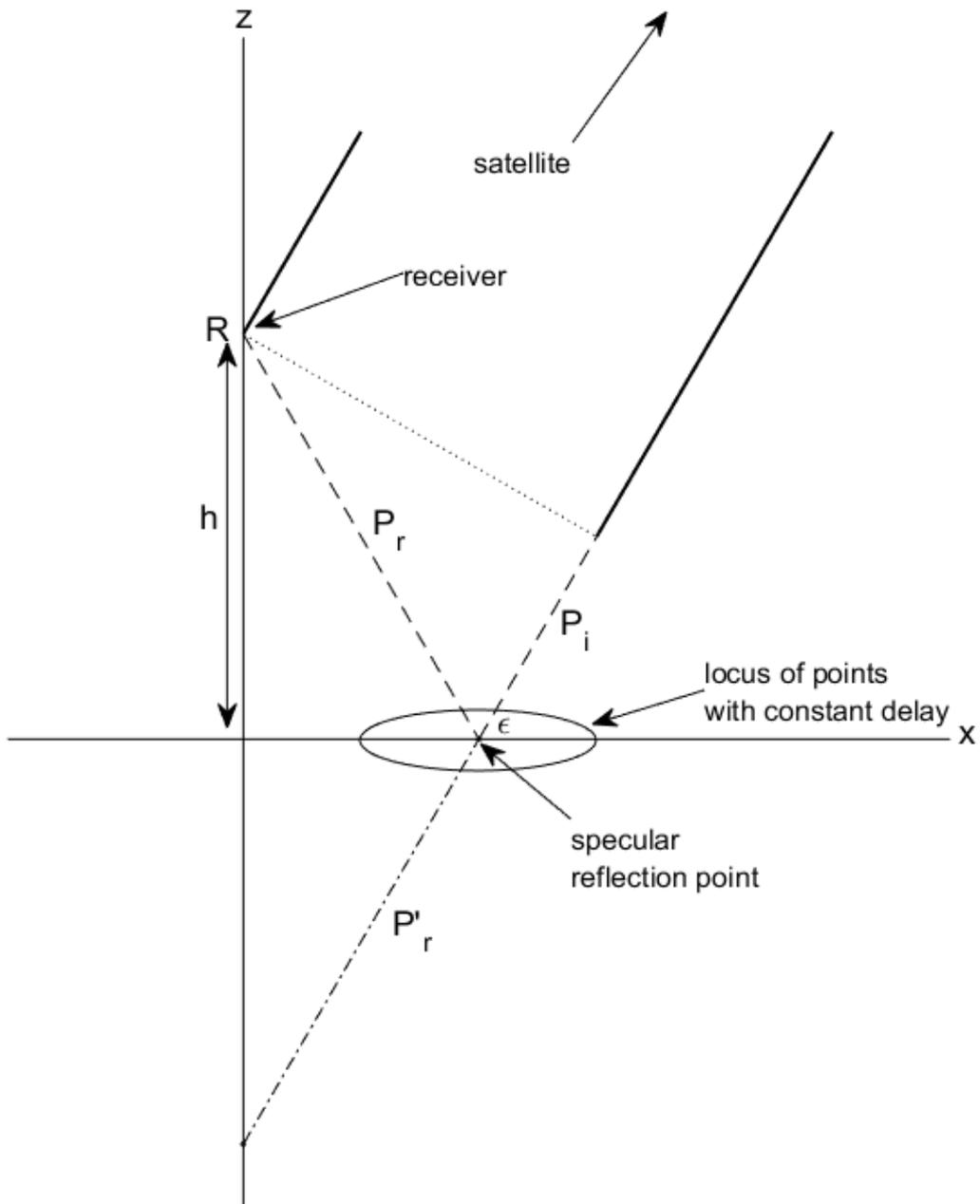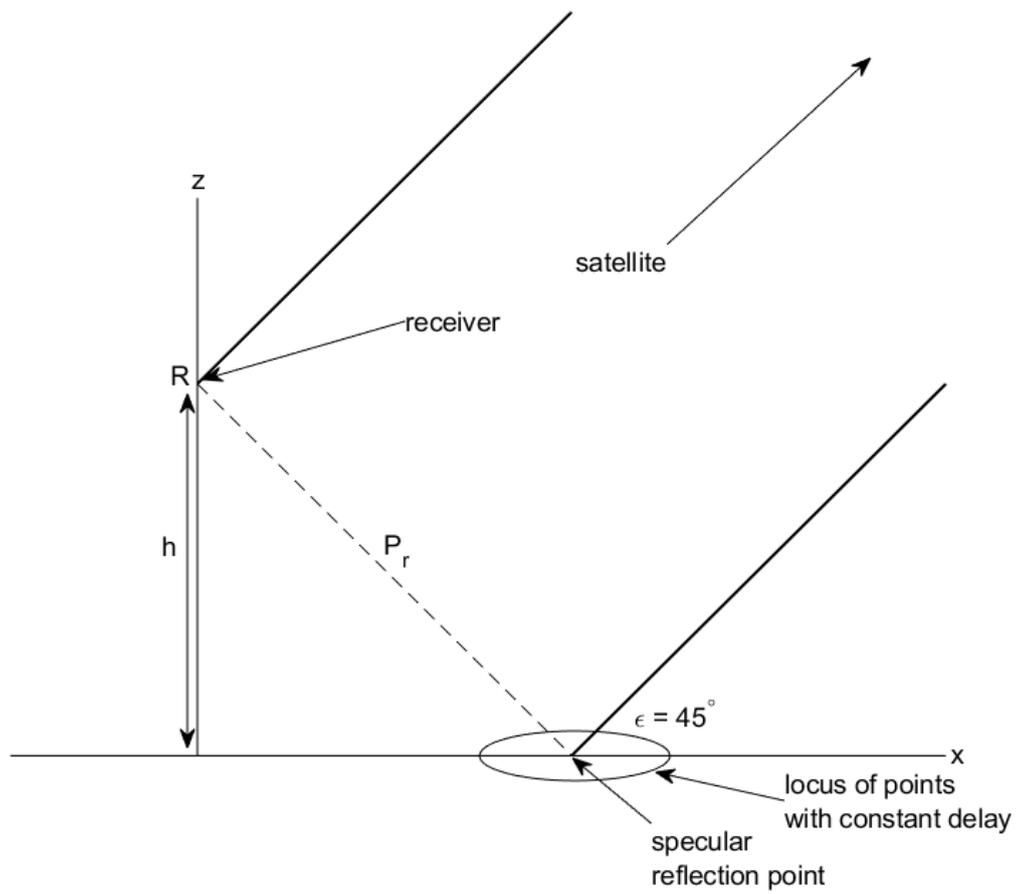$$\text{SNR}_{ref} = A\cos\left(\frac{4\pi h}{\lambda}\sin\epsilon + \varphi\right) \tag{2.13}$$

Figure 2.6: *The geometric relationship between receiver height h and multipath length when elevation angle ϵ is larger than 45°. Multipath length δ is equal to $P'_r - P_i$, receiver R is on the z-axis.*

n g

***Figure* 2.7:** *The geometric relationship between receiver height h and multipath length when elevation angle ϵ is 45°. Multipath length δ is equal to P_r, receiver R is on the z-axis.*

where λ is the carrier wavelength.

The SNR data in the Rinex file contain a mixture of direct and reflected data, which requires us to separate them before further processing. As noted by Bilich and Larson (2007), the long period component in the SNR data is due to SNR_{dir}, while multi-path creates smaller amplitude oscillations on top of the trend. It is worth to note that at lower elevation angles, the SNR value is smaller, and the oscillation amplitude is larger. To remove the SNR_{dir} from the SNR data, we use a low-order polynomial fit.
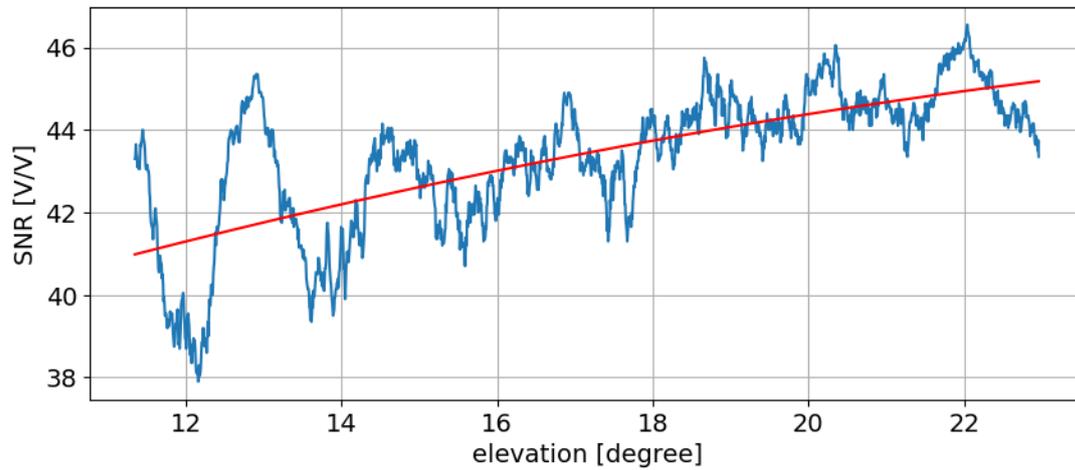
Figure 2.8: *The long period component is the direct SNR (red), which is modeled as a parabola and the oscillation on the trend is SNR from the reflected signal*
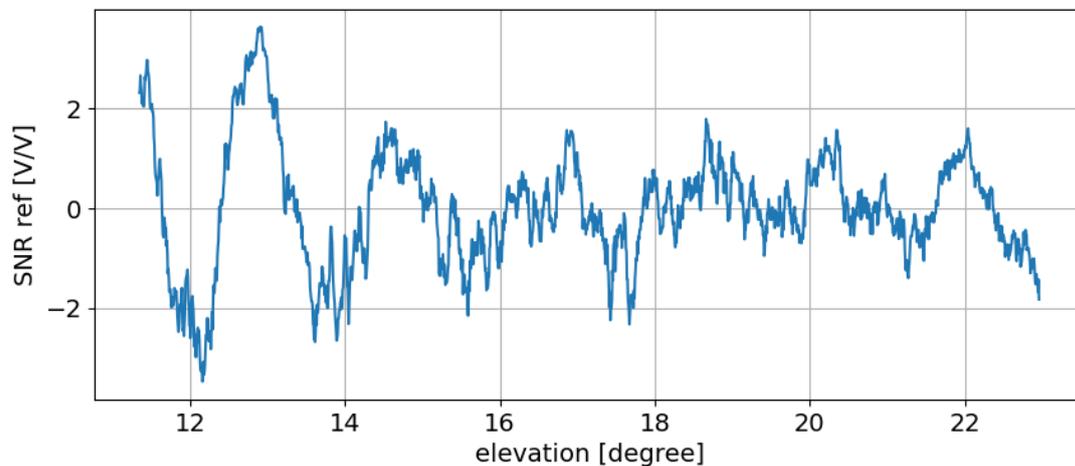
Figure 2.9: *After removing the long period component, the rest part is the SNR for reflected signals*

Equation 2.13 can be transformmed in

$$\text{SNR}_{ref} = A \cos\left(2\pi \cdot h \cdot \frac{2\sin\epsilon}{\lambda} + \varphi\right) \tag{2.14}$$

In Equation 2.14, the variable h can be interpreted as the frequency. As a result, algorithms such as Fourier transformation can be employed to extract the frequency h. However, it should be noted that the term $\frac{2\sin\epsilon}{\lambda}$ is not evenly sampled, making the Lomb-Scargle periodogram a more practical method for detecting the frequency h in the signal (Lomb, 1976; Scargle, 1982). The Lomb-Scargle periodogram can be viewed as a probability density function (VanderPlas, 2018), and the height can be extracted by locating the maximum likelihood, corresponding to the peak location.

Numerous studies have utilized the mentioned technique for monitoring sea and lake levels, and have extended its application in various contexts. For instance, Larson et al. (2017) discovered that systematic errors can arise when signals from low elevation angles are employed. Additionally, Santamaría-Gómez and Watson (2017) pointed out a misleading double peak phenomenon in the L2(P) signal-to-noise ratio (SNR) sequence, which can adversely affect the accurate extraction of frequencies. In response, Wang et al. (2019) proposed a multilayer decomposition combination method to mitigate the SNR noise. Furthermore, Strandberg et al. (2016) developed a new approach that employs a multi-parameter least squares fitting method to analyze the detrended SNR data, although this method may not be suitable for water level determination in poor environmental conditions. It should be noted that when the sampling rate is low and the distance between the antenna and reflecting surface exceeds a certain threshold, the detrended SNR becomes more complex (Song et al., 2019).

Chapter 3

Measurements and Data

3.1 Neckar River

The Neckar River is a significant right-bank tributary of the Rhine River, situated in south-western Germany [1]. With a total length of 367 kilometers, it originates in the Black Forest region and initially flows in a north and northeast direction. Upon reaching Plochingen, it transitions to a northwesterly course before passing through the city of Stuttgart [1]. The Neckar River holds significant geographical importance in the region, serving as a vital waterway for transportation, recreation, and supporting various ecological habitats in the surrounding areas. During the early 20th century, significant changes were made to the natural flow of the Neckar River between Plochingen and its mouth, resulting in the disappearance of the last freely flowing sections. This part of the river is now characterized by dammed areas, altering its natural state [2]. In the textured landscape of the Neckar region, the river valley became an important corridor for modern transportation infrastructure. The construction of railway lines and roads in the valley plains transformed the Neckar valley from a primarily cultural landscape into an industrial hub. Major companies such as Daimler AG and Mahle established their operations along the river, while recreational facilities like the Mercedes-Benz Arena and Cannstatt Wasen also found their place in this region between Plochingen and Bad-Cannstatt. These developments have shaped the modern identity of the Neckar area, combining industrial and recreational elements within its rich cultural and historical context[1].

The city center campus of the University of Stuttgart offers convenient access to a significant portion of the Neckar River through public transportation. However, it's important to note that certain sections of the river are restricted and require permission to enter due to their significance for shipping and water supply to the surrounding areas. To gain full access to these restricted areas, researchers are required to submit an application to the Wasserstraßen- und Schifffahrtsamt (WSA), the authority responsible for waterways and navigation. Once the application is approved by the WSA, researchers can conduct their activities legally and without interruptions, ensuring a smooth and compliant research process.

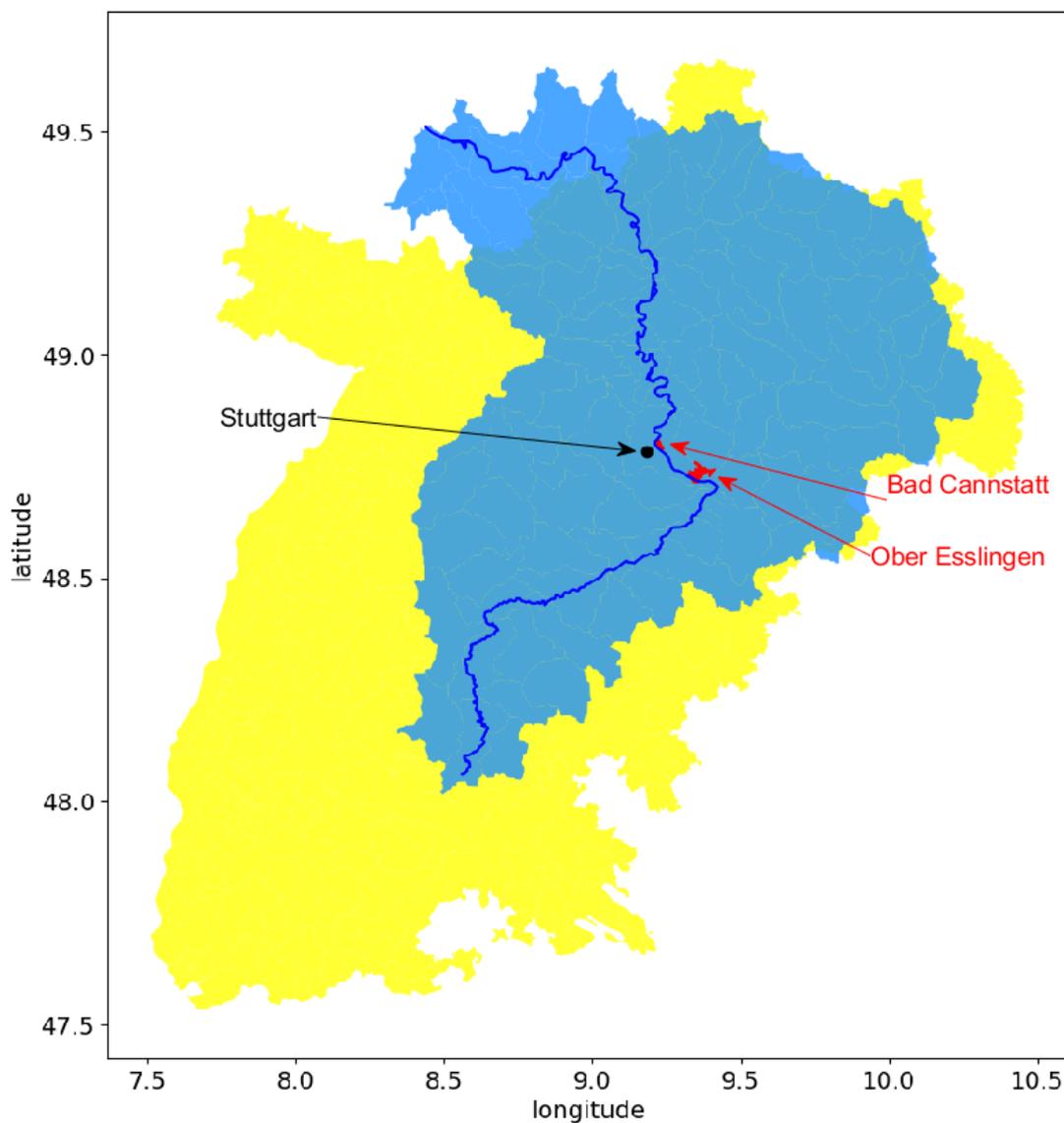
[1]https://www.britannica.com/place/Neckar-River
[2]https://de.wikipedia.org/wiki/Neckar

Figure 3.1: *The geographical representation indicates different regions: the yellow area corresponds to the state of Baden-Württemberg, the light blue area represents the catchment area of the Neckar River, and the deep blue line marks the course of the Neckar River itself. The black point signifies Stuttgart, the principal city of Baden-Wü̃rttemberg. Additionally, two red areas highlight the locations where the measurements were conducted.*

3.2 Measurements

3.2.1 Location

To compare the water level measurements obtained from Sentinel-3 and GNSS-IR, we conducted GNSS-IR measurements in areas where satellites pass overhead. In Stuttgart, specifically, Sentinel-3A flies over Ober Esslingen, while Sentinel-3B passes over Bad-Cannstatt. However, due to the approximate width of the river in these areas being around 50 meters, the signal from low elevation angles is prone to obstruction by the riverbank. Figure 3.2 illustrates the Fresnel zone for one station, indicating that the reflection zone of signals at an elevation of 10 degrees is already close to the river center. Consequently, multipath signals received within this elevation range may not originate from the water surface. Furthermore, the presence of numerous trees and buildings on the island located on the other side of the river can also obstruct the expected signals. As a result, we encountered challenges in obtaining valid results from stations situated on the riverbank.
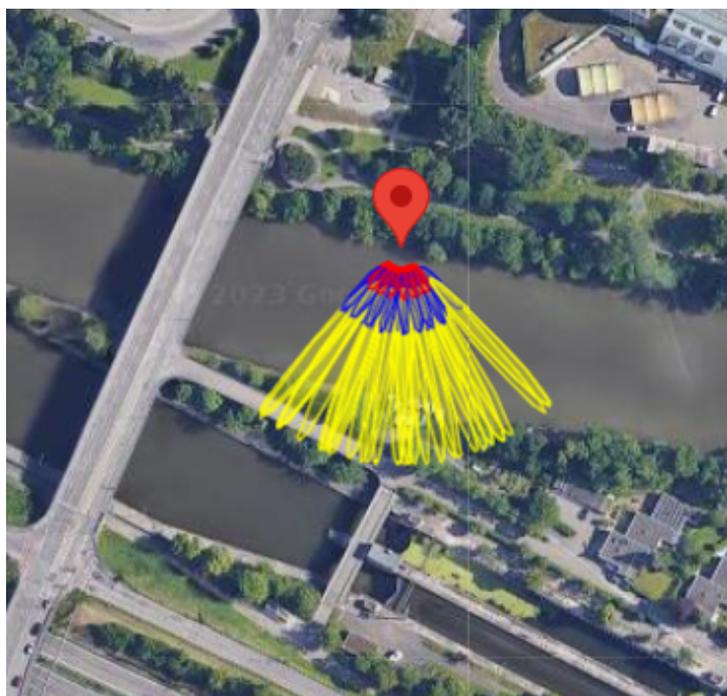
Figure 3.2: *Fresnel zone for a measurement station in Ober Esslingen with elevation at 5(yellow), 10(blue), 15(red) degree.*

In an effort to improve visibility of the river, we made attempts to install GNSS antennas on bridges. However, upon conducting the first Fresnel zone analysis for these bridge stations, as depicted in Figure 3.3, we encountered several challenges. As the vertical distance between the antenna and the water surface increased, the first Fresnel zone expanded in the horizontal direction, moving further away from the station. Consequently, the size of the ellipse representing possible reflected signals also grew larger. This indicates that the reflected signals originate from a broader area within the same elevation and azimuth range, making them more vulnerable to environmental factors such as nearby bridges. Unfortunately, despite

our efforts, the data obtained from these bridge stations did not yield valid results. Similarly, receivers positioned near sections of the river with bends observed rare occurrences of valid reflected signals. Furthermore, it is crucial to consider other factors such as avoiding locations with trees, buildings, and other tall obstructions. These objects not only block signals from the sky but also introduce additional reflected signals that are not from the water surface. Similarly, river sections with heavy ship traffic should be avoided as well.
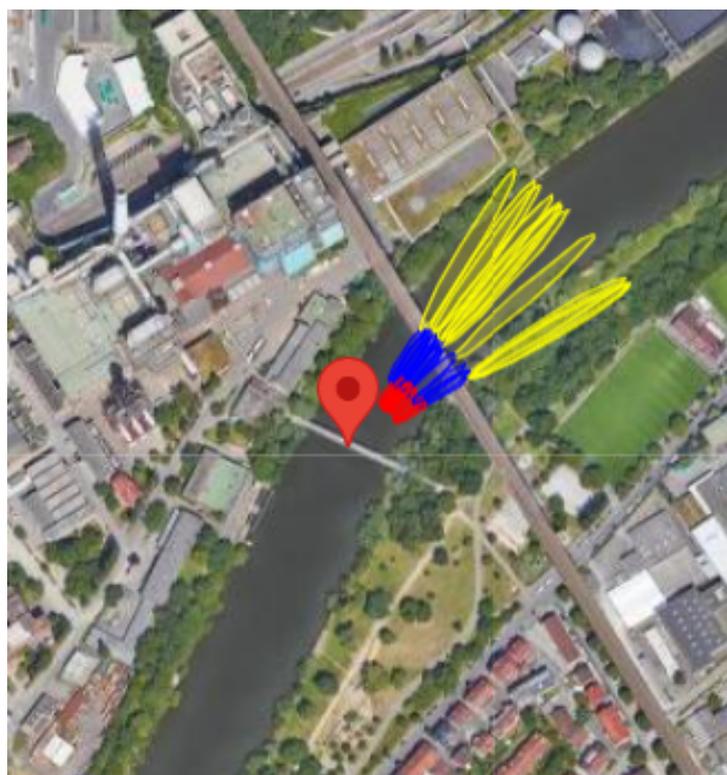
Figure 3.3: *Fresnel zone for a measurement station on a bridge in Bad-Cannstatt with elevation at 5(yellow), 10(blue), 15(red) degree.*

We conducted thorough testing of multiple locations in Ober Esslingen and Bad-Cannstatt to assess their suitability for our study. Unfortunately, the majority of these locations proved unsuitable due to the aforementioned challenges, as indicated by the red points in Figure 3.4. However, we were fortunate to receive permission to access a corner of the island in Ober Esslingen, marked by the green point in Figure 3.4. This particular location provided an unobstructed view of the river, allowing us to position the GNSS antenna as close to the water as possible, optimizing data collection as shown in Figure 3.5. Regrettably, despite our efforts, we were unable to find a suitable position in Bad-Cannstatt, which prevented us from comparing GNSS-IR and Sentinel altimetry measurements in that specific area. Nevertheless, the successful location in Ober Esslingen offers valuable insights for the comparison and validation of GNSS-IR and Sentinel altimetry measurements.
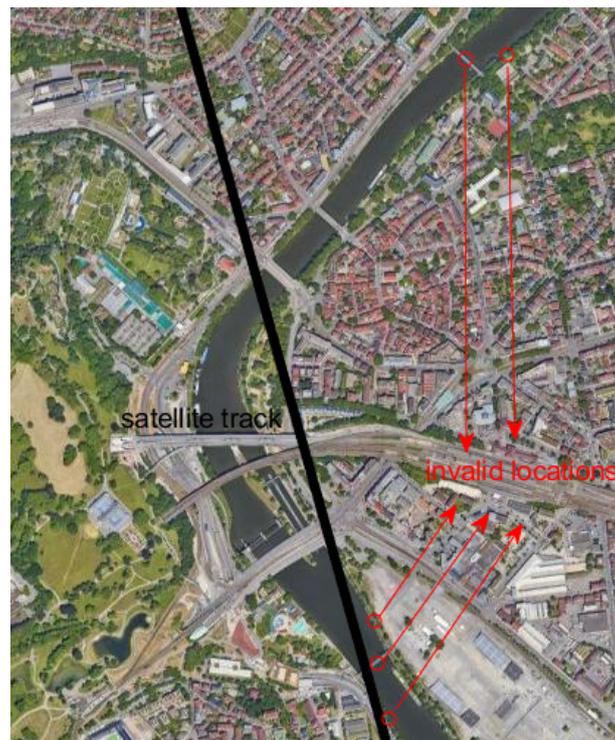
(a) Bad-Cannstatt
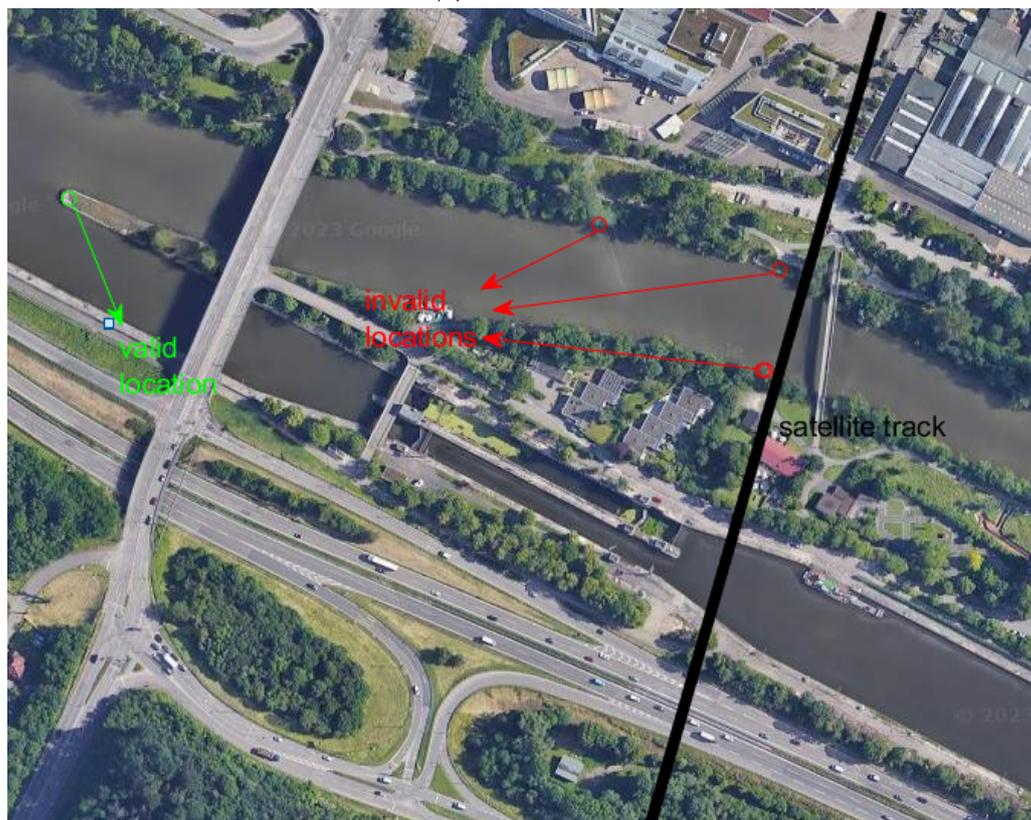
(b) Ober Esslingen

Figure 3.4: *Measurement stations in Ober Esslingen and Bad-Cannstatt, results from red points are proved to be invalid and all the valid measurements took place at the green point, the black lines in both figure are the satellite track projection.*

Figure 3.5: *A picture for the location where the measurement took place, the measurement site was carefully chosen at the river center to provide an optimal line of sight to the river. This location offered excellent visibility and a clear view of the river. Moreover, the antennas were positioned near the surface, ensuring their close proximity to the water for accurate and reliable measurements.*

3.2.2 Setups

In compliance with water and sailing protection regulations, certain areas along the Neckar river were restricted from access. However, all the measurements conducted as part of this study were approved by the WSA (Wasserstraßen- und Schifffahrtsamt), as mentioned in section 3.1.

During the measurement process, it is crucial to use an appropriate mode to ensure accurate positioning. Signals from low elevations can negatively impact positioning accuracy, leading many receivers to filter out these signals. Unfortunately, in the initial 5 campaigns, these signals were inadvertently excluded from our measurements. To track a greater number of signals, we modified the receiver settings to allow for the reception of signals from 3 GNSS systems, as described in detail in section 3.3. Additionally, we set a high sampling rate of 1 second to avoid any distance limitations. It is essential to consistently double-check these details in future work to ensure accurate and reliable measurements.

The Sentinel-3A satellite passes over the Neckar river in Ober Esslingen approximately every 27 days at 10:02 UTC. During several early measurement campaigns, a pair of leveled Leica GS15 antennas were utilized, serving as a reference to ensure measurement reliability. However, on February 16th and March 15th, 2023, for improved positioning accuracy, one Leica GS25 antenna was incorporated, while one of the Leica GS15 antennas was rotated to optimize the reception of reflected signals. The remaining setup parameters were consistent across all measurements, including a data sampling rate of 1 second and tracking of signals

from GPS, Glonass, and Galileo satellite systems. More specific details can be found in Table 3.1. These standardized settings allow for consistency and comparability in the collected data, facilitating accurate analysis and interpretation in subsequent research.

Date	Antenna settings	duration
11/08/2022	2 Leica GS15	2 hours
07/09/2022	2 Leica GS15	2 hours
04/10/2022	2 Leica GS15	2 hours
31/10/2022	2 Leica GS15	2 hours
27/11/2022	2 Leica GS15	2 hours
16/02/2023	1 Leica GS15 + 1 Leica GS25	6 hours
	1 Leica GS15 + 1 Leica GS25 (rotate)	2 hour
15/03/2023	1 Leica GS15 + 1 Leica GS25 (rotate)	6 hours

Table 3.1: *measurement campaign setups, sampling rate is 1 second and all signals (see Table 3.2) are received.*

3.2.3 Antenna Rotation

The minimum gain beamwidth and the rate of gain variation in the elevation plane of a GNSS antenna play crucial roles in determining the number of satellites that can be tracked effectively at different elevation angles. GNSS antennas, including geodetic antennas, are typically designed with a broadside direction that offers maximum gain and optimal polarization properties when aimed at the zenith or directly overhead.

However, as the elevation angle decreases and the satellite moves towards the horizon, the gain of the antenna diminishes rapidly. This decrease in gain can be quite significant, with values as large as 10dB reported in the literature (Rao et al., 2013). Consequently, the antenna's ability to effectively track and receive signals from satellites at lower elevation angles is significantly compromised. When planning and conducting satellite tracking activities, it is crucial to consider these characteristics of GNSS antennas. Understanding the antenna's gain pattern and the variation in the elevation plane enables researchers and engineers to optimize satellite tracking strategies and ensure reliable and accurate reception of GNSS signals, especially when dealing with satellites at lower elevation angles.
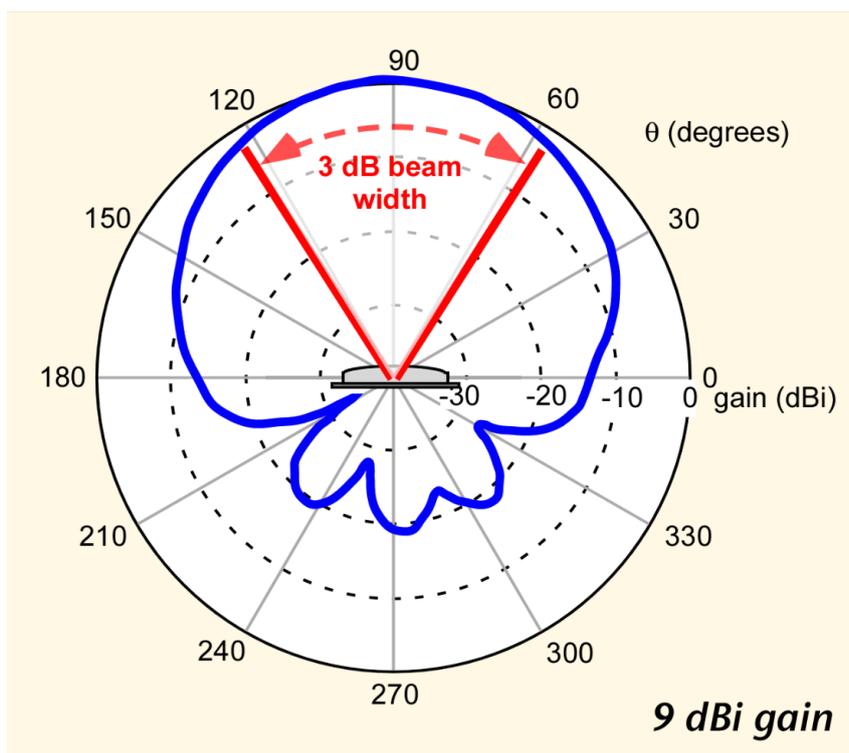
Figure 3.6: *Antenna diagramm shows the gain pattern for a GNSS antenna. Image source: https://en.wikipedia.org/wiki/File:Patch_antenna_pattern.gif*

In GNSS-IR studies, the signals reflected from "under" the horizon, particularly those from the water surface, are of focus. To enhance the reception of these signals, researchers have explored different approaches. One such approach, as discussed in a study by Purnell et al. (2021), involves rotating the GNSS antenna so that its top faces the water surface. By adjusting the antenna orientation in this manner, researchers aim to optimize the reception of the reflected signals, improving the quality and accuracy of the results obtained. In your own measurement campaigns, as outlined in Table 3.1, we have also implemented this method to enhance the quality of the data collected.

To maintain stability, the rotated antenna was securely fixed on the tripod by taping the Leica GS15 antenna body, as depicted in Figure 3.8. However, due to its unique shape, the Leica GS25 antenna could not be fastened to the tripod when rotated.

During the measurement campaign on February 16th, the Leica GS15 antenna was rotated for a duration of 2 hours. It is important to note that rotating the antenna can result in an increased reception of multipath signals compared to normal conditions. This rise in multipath signals may impact the accuracy of the positioning, posing challenges for accurately determining the absolute height of the water level. To address the challenges encountered during the rotated antenna measurements, a different approach was implemented on March 15th. The Leica GS25 antennas were used as the positioning antennas, offering improved accuracy. A reference point was established on the tripods, and the distance between the antenna phase center and the tripods was measured using a ruler. The measurements were conducted in two phases. In the first phase, the Leica GS25 antenna was positioned on tripod

1 in a leveled configuration, while the Leica GS15 antenna was rotated on tripod 2. After a duration of 3 hours, the antennas were switched, with the Leica GS25 antenna placed on tripod 2 in a leveled configuration, and the Leica GS15 antenna rotated on tripod 1 (Figure 3.7). This setup allowed for the determination of the ellipsoidal height of the rotated antennas by utilizing the temporal reference and the Precise Point Positioning (PPP) solution obtained from the leveled antenna.

By employing this method, the rotated antenna's ellipsoidal height can be accurately determined, improving the overall accuracy and reliability of the water level estimation derived from the GNSS-IR measurements.

$$H_{\text{rotate}} = H_{\text{level}} - dH_{\text{level}} + dH_{\text{rotate}} \tag{3.1}$$

where H is the phase center height in WGS84 system and dH the height offset to the reference.
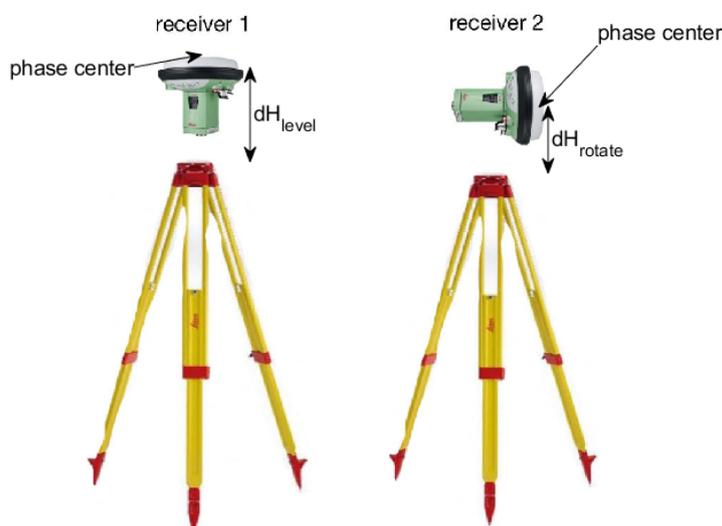
Figure 3.7: *Receiver 1 was initially used for positioning, and after three hours of measurement, the other receiver was set up on the same tripods but with a different rotation position. To accurately determine the absolute position of the rotated receiver, the offset between the phase center of the receiver and the tripods was measured. This offset measurement enabled the calculation of the precise position of the rotated receiver relative to the tripods. By obtaining the absolute position of the rotated receiver, it was possible to further analyze and compare the data collected from both receivers in the study.*

Figure 3.8: *To ensure stability and proper orientation, the antenna was rotated so that its top surface faced the water. Additionally, it was securely taped onto the tripods to maintain stability throughout the measurement period. This setup allowed for consistent and reliable data collection without any disturbance or unintended movement of the antenna.*

3.3 GNSS Signal

As outlined in section 3.1, Neckar River is narrow and thus poses a significant limitation for GNSS-IR measurements. To overcome this limitation and increase the number of valid measurements, we utilized signals from three different GNSS systems: GPS (Global Positioning System) from the United States, GLONASS (Global Navigation Satellite System) from Russia, and Galileo from the European Union. Table 3.2 provides a list of the selected signals along with their corresponding frequencies. This comprehensive approach allowed us to capture a broader range of GNSS signals and maximize the data available for the analysis, ultimately improving the accuracy and robustness of our results.

GNSS System	Signal	Frequency (MHz)
	L1	1575.42
GPS	L2C	1227.60
	L5	1176.45
Glonass	L1	$1602 + k \cdot 0.5625$
	L2	$1246 + k \cdot 0.4375$
	E5a	1176.45
Galileo	E6	1278.70
	E5b	1207.14
	E5	1191.795

Table 3.2: *GNSS signal systems with frequencies, in GLONASS system, signal frequency related to the channel number k*

GLONASS, unlike GPS and other GNSS systems, utilizes FDMA (Frequency Division Multiple Access) for its legacy signal transmission. In the GLONASS constellation, each satellite is assigned a unique frequency in the L1 and L2 bands. The channel numbers assigned to each GLONASS satellite can be found in Table 3.3.

Channel k	-7	-4	-3	-2	-1	0	1	2	3	4	5	6
Satellite index	14,10	2,6	18,22	9,13	12,16	11,15	1,5	20,24	19,23	17,21	3,7	4,8

Table 3.3: *Glonass channel-number pair, channel -6 and -5 are for test purpose and not in real application.*

To implement GNSS-IR solutions, we utilized TEQC, a freeware program designed to support various tasks in GNSS data processing. TEQC offers a range of functionalities, including translating binary receiver formats to the standardized Rinex (Receiver Independent Exchange) format, editing existing Rinex files, and conducting data quality checks prior to post-processing (Estey and Meertens, 1999). By leveraging TEQC, we easily converted the binary raw data into the Rinex2.11 format, calculated azimuth and elevation angles, and extracted the necessary SNR data for our analysis. We have provided the commands for performing these operations in Appendix C.

3.4 Altimetry Data

Sentinel-3 is an ongoing mission by the joint program of ESA and EUMETSAT at an inclination of 98.65°. The spacecraft is equipped with 4 main instruments including SRAL which is the SAR RADAR Altimeter. It emitts pulses within the Ku band at 15.575 GHz and C band at 5.42 GHz and provides Low Resolution Mode (LRM) and Synthetic Aperture Radar (SAR) mode[3]. For the analysis of altimetry level-2 data obtained from Sentinel-3A, a specialized software developed by the Geodetic Institute of the University of Stuttgart is employed. This software is designed to process non-time critical altimetry data from the Sentinel-3 mission and provides water level estimations in the WGS84 coordinate system. The software incorporates various retracking methods, including ocean retracker (for LRM and SAR), offset centre of gravity retracker (for SAR), ice retracker (for LRM) and sea ice retracker (for SAR).

The main objectives of the Sentinel-3 level-2 processing data is to provide elementary retracked altimeter estimates of the ocean, coastal zones, ice sheet, and sea-ice elevation, there are different re-tracking algorithm that are applied:

- Ocean retracking of SAR mode: Inherited from the SAMOSA project, a methodology is employed to fit the theoretically modeled multi-look L1B waveform to the real L1B Synthetic Aperture Radar (SAR) waveform. This fitting process enables the estimation of essential parameters. [4]

- Ocean retracking of LRM mode: Inherited from the JASON-2 mission[5], a fitting technique is employed to analyze and characterize the waveform data using a 4th parametric model

---

[3]https://sentinels.copernicus.eu/web/sentinel/missions/sentinel-3/instrument-payload/altimetry

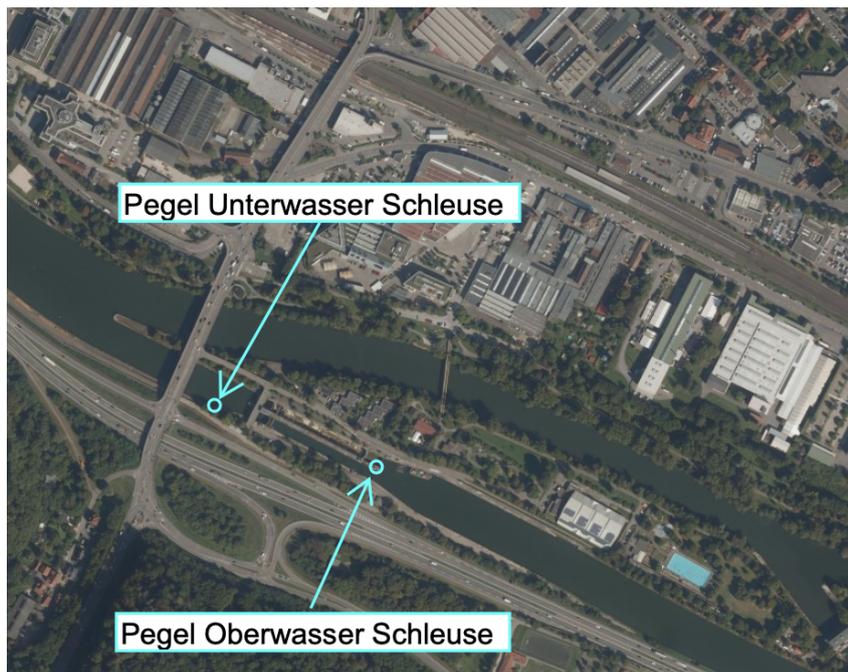[4]https://sentinels.copernicus.eu/web/sentinel/technical-guides/sentinel-3-altimetry/level-2/re-tracking-estimates/ocean

[5]https://www.jpl.nasa.gov/missions/jason-2

estimation. By performing this fitting, valuable information about the waveform can be obtained, including features such as the peak amplitude, leading edge and trailing edge.
[4]

- OCOG of SAR mode: Heritage of the ice-1 re-tracker implemented in both ENVISAT[6] and CryoSat-2[7] missions. It is an empirical-based algorithm used in LRM mode for ice surfaces and in SAR mode for sea-ice margins. This method is based on the OCOG and requires form the estimation of the waveform amplitude as it is using a threshold-based approach to infer the epoch. Then, OCOG amplitude is estimated.[8]

- Ice sheet retracking of LRM mode: The Maximum Likelihood Estimation (MLE) technique is utilized to perform a fitting of the waveform with a 4th order parametric model. The MLE approach aims to find the parameter values that maximize the likelihood of the observed waveform data given the assumed parametric model.[9]

- Ice sheet retracking of SAR mode: The method is that used for waveforms received in the SARin degraded case for the CryoSat-2 mission. The retracking algorithm has been designed to exploit least squares fitting of a semi-analytical model of the echo. The echo model is a modified gaussian form. It corresponds to a six parametrizable function with 5-section modelling.[9]

- Ice retracking of LRM mode: Heritage of the ice-retracker (also called ice_erf retracker) implemented in both ENVISAT and CryoSat-2 missions. It is a physical-based retracker.[10]

- Sea ice re-tracking of SAR mode: Heritage in the empirical-based sea-ice re-tracker implemented in the CryoSat-2 mission. It corresponds to a simplified version of the 5-sections ice-sheet retracker used in CryoSat-2. In this case only three segments are considered: leading edge is modelled as a Gaussian; an exponenetial function is used to fit the trailing edge decaying; and a third order polynomial function.[11]

3.5 Gauge Data

To provide accurate data on water levels in the study area, we were fortunate to have access to a nearby gauge station. Through individual requests, we obtained water level data from the WSA for the period prior to November 2022 in Ober Esslingen (see Figure 3.9). This data is sampled at a frequency of every 15 minutes and is available in the DHHN2016 height system. The height offset between DHHN2016 and WGS84 frame is already known and the transformation can be done. Thus the gauge data can be compared with other data sources.

---

[6]https://earth.esa.int/eogateway/missions/envisat

[7]https://www.esa.int/Space_in_Member_States/Germany/Die_Forschungsfracht_von_CryoSat-2

[8]https://sentinels.copernicus.eu/web/sentinel/technical-guides/sentinel-3-altimetry/level-2/re-tracking-estimates/ocog

[9]https://sentinels.copernicus.eu/web/sentinel/technical-guides/sentinel-3-altimetry/level-2/re-tracking-estimates/ice-sheet

[10]https://sentinels.copernicus.eu/web/sentinel/technical-guides/sentinel-3-altimetry/level-2/re-tracking-estimates/ice

[11]https://sentinels.copernicus.eu/web/sentinel/technical-guides/sentinel-3-altimetry/level-2/re-tracking-estimates/sea-ice

Figure 3.9: *Several gauge stations are distributed around the water dam, we will use the water level measured at "Unterwasser Schleuse" as reference because the water level here should be very close to the GNSS-IR footprint.*

The gauge station data serves as a valuable complement to the altimetry data from Sentinel-3A and the GNSS-IR measurements, offering additional insights into the water level dynamics in the study area. By integrating this data into our analysis, we can achieve a comprehensive understanding of the water levels and further enhance the accuracy and reliability of our research findings.

Chapter 4

Method

4.1 Periodogram Multiplication

In many previous studies, the focus has been on analyzing the long-term trends in water surface height, which often involves daily data processing. However, in our study, the main objective is to compare the results from GNSS-IR and satellite altimetry using Sentinel-3A. Since Sentinel-3A passes over the Neckar river in less than one second, we only have a limited amount of data available during each satellite pass. Consequently, we aim to find a method that allows us to analyze the collected data with higher time resolution. This can be achieved by multiplying the periodogram generated from LSP using a moving window.

After filtering the data based on a predefined azimuth and elevation range, we implemented a time window approach with a specific duration (e.g. 30 minutes). This time window was then systematically applied throughout the entire measurement period. Within each time window, we extracted the SNR data and performed Lomb-Scargle Periodogram (LSP) analysis separately for different signals received from different satellites. By multiplying the individual periodograms obtained within each time window, we effectively combined the information from multiple satellites with signals reflected from different directions and use it as the result for the mid point in the chosen time window. This approach offered several advantages. Firstly, it allowed us to reduce the influence of signals that were not actually reflected from the water surface, enhancing the accuracy of the analysis. Secondly, it enabled us to capture the height difference between the antenna phase center and the water surface, treating it as the height at the midpoint of the time range. By shifting the time window and repeating this process, we generated a time series with a higher time resolution. The resolution was determined by the extent to which we moved the window for each iteration. This approach facilitated the creation of a more detailed time series, allowing for a comprehensive comparison between the GNSS-IR and satellite altimetry results with enhanced temporal resolution.

LSP can be regarded as a probability density function (VanderPlas, 2018), thus we are able to use the interquartile range (IQR) for the multiplied periodogram as the accuracy for water level at each single window. After that, we can compute the error for the whole timeseries using error propagation.

In this specific example, we analyzed the data collected between 11:30 and 12:00 on March 15th, utilizing a time window of 30 minutes. With the antenna positioned approximately 3 meters above the water surface, our focus was on the frequency range between 2 and 6 meters. During this time range, we observed signals from two GPS satellites and one Galileo satellite,

resulting in a total of nine signals. Among these signals, the data from satellite G28 exhibited poorer quality compared to the signals from the other two satellites. Additionally, the L1 signal from satellite G31 appeared weaker than the other signals. To extract the desired information, we performed a multiplication process on the nine individual periodograms obtained from each signal, as illustrated in Figure 4.2. This multiplication revealed a prominent peak at a height of approximately 2.67 meters, corresponding to the midpoint of the valid peaks observed in Figure 4.1. The presence of this clear peak indicates a strong reflection from the water surface at that specific height.
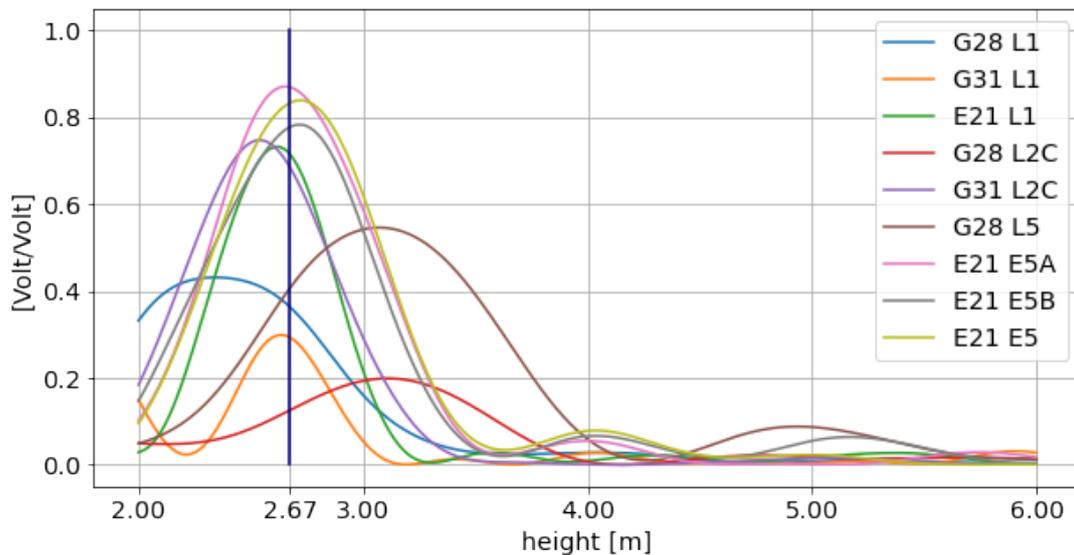
Figure 4.1: *All Lomb Scargle periodogram from 11:30 to 12:00 on 15 March.*
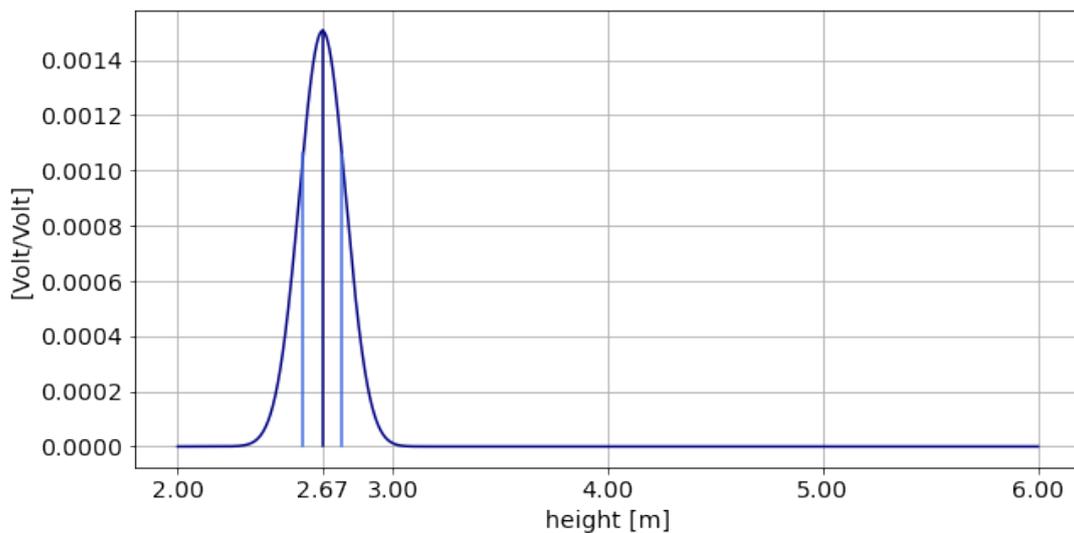
Figure 4.2: *Multiplied periodogram using the LSP in Figure 4.1, the light blue lines present the uncertainty range using IQR.*

Indeed, there are instances where the analysis of the multiplied periodogram may not produce a perfect result. An example of this can be seen in Figure 4.3 at 11:58, representing a time window from 11:43 to 12:13. In this case, the peak location in the multiplied periodogram is observed at a greater height than expected. This discrepancy can be attributed to the influence of specific signals, such as E19 L1, E19 E5B, E19 E5, R02 L1, and R02 L2.
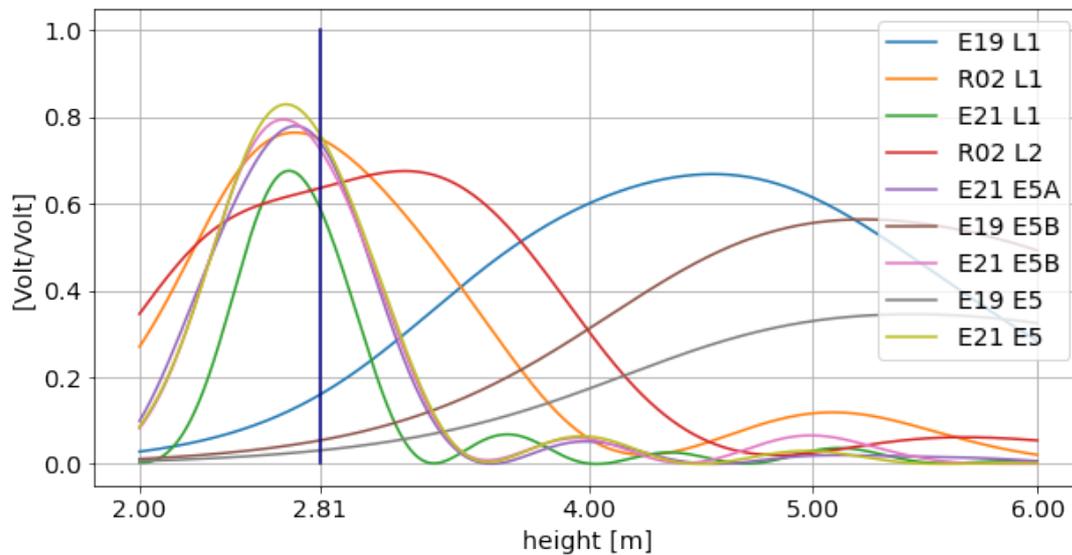
Figure 4.3: *In the Lomb-Scargle periodogram analysis conducted from 11:43 to 12:13 on 15 March, the resulting peak in the multiplied periodogram diverged from the peaks observed in most of the original Lomb-Scargle periodograms.*

During the measurement period on February 16th, a time series (Figure 4.4) was generated using the rotated antenna GS25 and the analysis approach described earlier. By applying an elevation range of 5 to 30 degrees and an azimuth range of 270 to 330 degrees, and utilizing a time window with a length of 30 minutes, the resulting time series provided an estimation of the water surface height variation throughout the measurement period. Each data point (represeting each time window midpoint) in the time series represented the estimated height at a specific time, based on the analysis of the GNSS-IR signals. If it becomes possible to receive data from satellites across a larger azimuth range, a continuous time series can be generated. With a sufficiently long observation, this time series could offer a high-resolution representation of the temporal dynamics of the water surface height, enabling a detailed examination of the fluctuations and trends within the Neckar River. Such insights would be valuable for understanding the behavior of the water level during the specific measurement period and beyond.
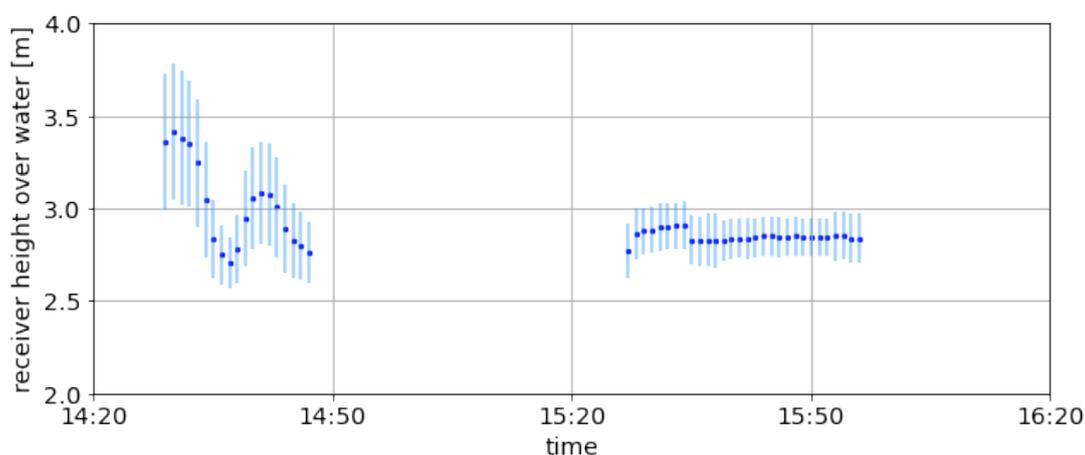
Figure 4.4: *Antenna height with errors over water surface time series of rotated antenna on16 February using azimuth range 270 to 330 degree, elevation range 5 to 30 degree and time window length 30 minutes*

The estimated height between the antenna phase center and the water surface was approximately 2.91 meters. It is worth noting that the narrow range of azimuth and elevation angles used in the filtering process resulted in significant data gaps within the time series. To address this issue and fill in the gaps, it is possible to expand the range of the azimuth and elevation angle filters. However, it is crucial to consider that increasing or decreasing the range may introduce more errors, as it would include or exclude signals from a wider range of sources beyond the water surface, especially when the environment is complicated. This potential trade-off between data completeness and reliability will be further investigated through iterative processes with different settings, which will be discussed in detail in chapter 5.

4.2 Positioning

In this study, we employed an open-source software called PRIDE[1] (Geng et al., 2019) to conduct Precise Point Positioning (PPP) solutions for the provided RINEX file. The software utilizes the WGS84 ellipsoid and calculates the coordinates in the ECEF (Earth Center Earth Fixed) system with centimeter-level accuracy.

To obtain the ellipsoidal height, we applied a transformation method described in Appendix A. The transformation allowed us to convert the ECEF coordinates to the ellipsoidal height, providing a more meaningful representation of the vertical position.

For the majority of the measurement campaigns, the positioning point was not set at the antenna phase center. Consequently, an offset needed to be considered when determining the water level based on the antenna position. The antenna heights for each campaign are provided in Table 4.1.

---

[1]https://github.com/PrideLab/PRIDE-PPPAR

Date	Antenna Number	Positioning Point Height	Offset	Phase Center Height
11/08/2022	1	287.45	0.20	287.65
	2	287.44	0.20	287.64
07/09/2022	1	287.34	0.20	287.54
	2	287.47	0.20	287.67
04/10/2022	1	287.39	0.20	287.59
	2	287.36	0.20	287.56
31/10/2022	1	287.45	0.20	287.65
	2	287.47	0.20	287.67
27/11/2022	1	287.41	0.20	287.61
	2	287.42	0.20	287.62
16/02/2023	1	287.47	0.20	287.67
	3	287.23	0	287.23
	1r	287.25	NaN	287.25
15/03/2023 phase 1	1r	NaN	NaN	287.30
	3	287.50	0	287.50
15/03/2023 phase 2	1r	NaN	NaN	287.29
	3	287.49	0	287.49

Table 4.1: *Ellipsoidal antenna height of each measurement campaign in WGS84 frame, antenna 1 and 2 are Leica GS15 antennas and 3 is an Leica GS25 Antenna. r means the antenna was rotated during the measurement. Red marker means the height is calculated direct using the measured data from rotated antenna, which is very inaccurate, blue marker means the height is determined using another antenna (see Equation 3.1)*

.

Chapter 5

Results

5.1 Determine the Best Setting

Using the methods introduced by chapter 4, we are able to generate water level time series during the whole measurement campaign. To get the best results, we need to define the best configuration for our analysis including azimuth range, elevation range and time window length.

5.1.1 Azimuth Range

It is relatively easy to define the azimuth range, we can plot the first Fresnel Zone of our receivers since we are familier with the environment, approximate antenna height. Using the web software from Roesler and Larson (2018) [1], we plotted the first Fresnel Zone in Figure 5.1.
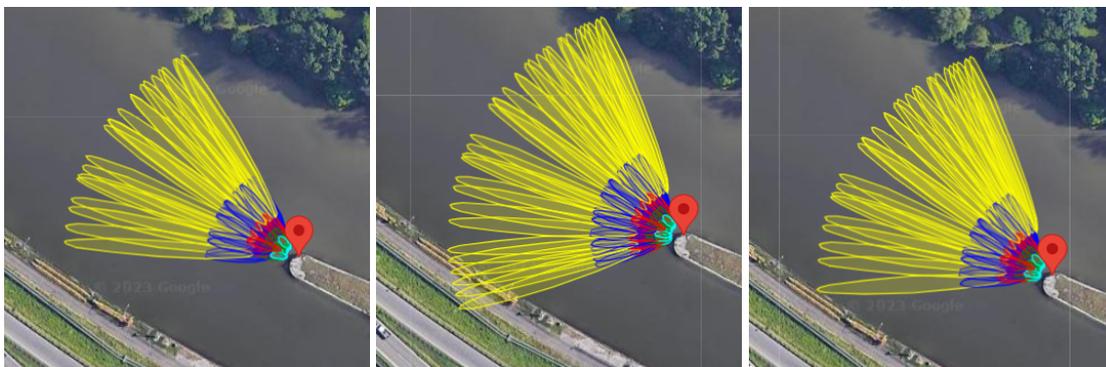
(a) Azimuth from 270 to 330 degree   *(b) Azimuth from 250 to 350 degree*   *(c) Azimuth from 265 to 340 degree*

Figure 5.1: *First Fresnel Zone in the location, yellow, blue, red ,green, cyan are for elevation 5,10,15,20,25 degree approximate receiver height is set to 3 meter*

The selection of the azimuth range is indeed a crucial factor in capturing valuable signals while minimizing noise and unwanted reflections. Based on the observations in Figure 5.4, it appears that choosing an azimuth range of 75 degrees, as shown in Figure 5.1c, strikes a reasonable balance between data availability and potential noise sources. In Figure 5.1a, where only signals from a limited portion of the sky are tracked, there is a possibility of missing valuable signals. On the other hand, in Figure 5.1b, a wider azimuth range is used, but it

---

[1]https://gnss-reflections.org/rzones

includes signals from the riverbank and other areas that may introduce additional noise and unwanted reflections. By selecting an azimuth range of 75 degrees, we have avoided the signals from the riverbank while still capturing a significant portion of the available signals. Although the yellow ellipse edge is close to the riverbank, it appears that this configuration does not introduce significant noise or unwanted reflections.

However, it is important to note that the selection of the azimuth range is dependent on the specific characteristics of the study area and the desired trade-off between data availability and noise sources. It is always recommended to carefully evaluate the impact of different azimuth ranges and adjust the configuration as needed based on the observed results and the specific requirements of the study.

5.1.2 Elevation Range & Time Window Length

Both the elevation range and the time window length play significant roles in determining the quality of our method, and therefore, it is crucial to consider these two parameters simultaneously. For our analysis, we selected the observation data from September 7th to conduct a test.

When searching for an appropriate elevation angle range, our primary focus was on identifying the optimal maximum elevation. This is because signals from low elevation angles are particularly valuable for GNSS-IR measurements. In the initial five campaigns, we maintained an elevation filter of $10°$, meaning that only signals with elevations higher than $10°$ were included. To determine the best maximum elevation angle, we started with $25°$, following the approach used in previous studies. We then gradually increased the angle, testing each degree increment until reaching $50°$. Given the proximity of our antenna to the water surface, we expected that signals reflected at this elevation would predominantly originate from the water surface itself.

The length of the time window is another critical parameter that significantly affects the quality of our analysis. If the window is too short, there may not be enough data for the Lomb-Scargle Periodogram (LSP) to accurately determine the correct height. On the other hand, if the time window is too large, we face two challenges. Firstly, there may be a scarcity of results, especially when we have limited observation data for a particular satellite. For example, if we have only 45 minutes of observation from a single satellite and set a 45-minute time window, we can only extract the height at one specific time point from that satellite. Secondly, a larger time window corresponds to a longer satellite footprint track on the Earth's surface. Consequently, the height difference between the receiver and the reflection surface varies over this extended time, which can adversely affect the LSP results. To determine the optimal time window length, we began with a 15-minute window and incrementally increased it by 1 minute until reaching 45 minutes.

Through analyzing the mean height, standard deviation, and the number of valid height estimates, we can identify the best configuration for our final analysis.
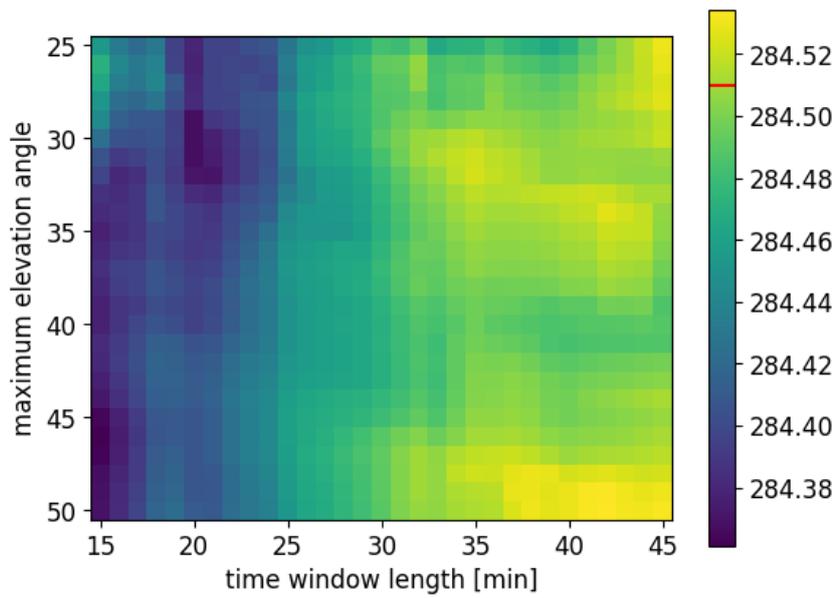
Figure 5.2: *Mean water level using different maximum elevation angle and time window length for leveled receiver. The gauge value is marked on the colorbar as red line.*
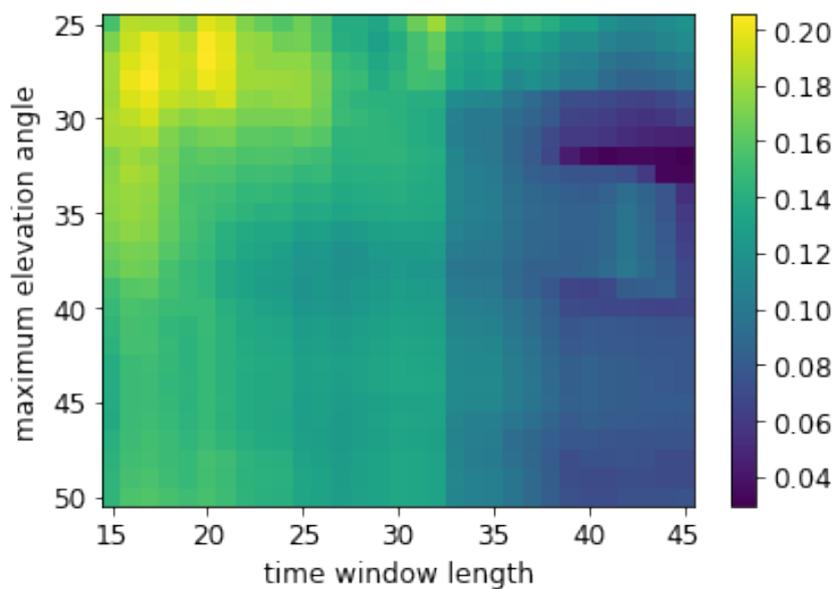
Figure 5.3: *Standard deviation using different maximum elevation angle and time window length for leveled receiver*
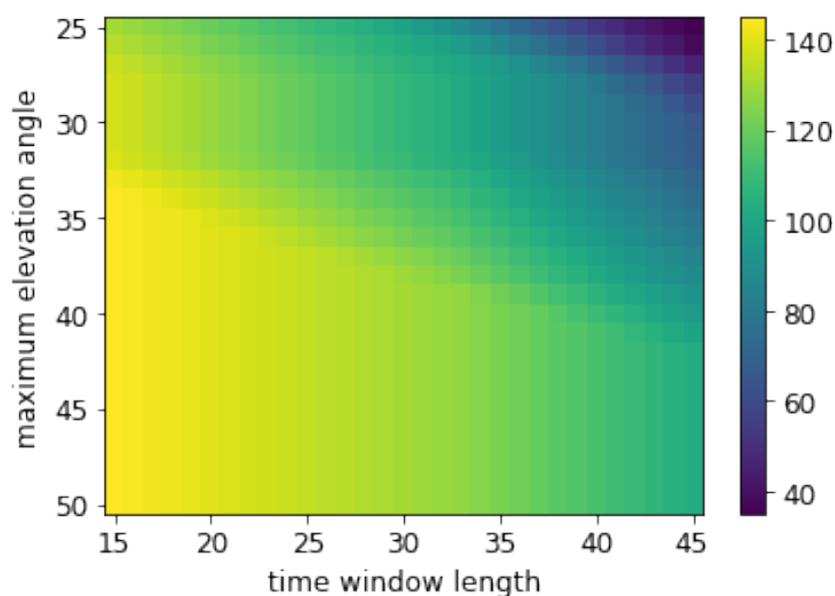
Figure 5.4: *Point number using different maximum elevation angle and time window length for leveled receiver*

In Figure 5.2, the water level based on the gauge measurement (284.51 m) is indicated on the colorbar. The plot shows that when the time window is less than 30 minutes, there is a significant difference between the mean value and the gauge value, and the standard deviation is also larger, indicating a lack of stability in the time series. However, as the time window increases to more than 35 minutes, the standard deviation initially decreases and then starts to increase with higher maximum elevation angles. The standard deviation reaches its minimum value around 32° maximum elevation, and the mean height at this elevation is also close to the gauge value.

As shown in Figure 5.4, to minimize gaps in the time series, it is beneficial to increase the maximum elevation angle and choose a shorter time window. This approach allows us to utilize as much data as possible for the analysis. By increasing the maximum elevation angle, we can capture signals from a wider range of elevation angles, leading to a more robust time series. Similarly, selecting a shorter time window ensures that we produce a higher density of data points from the analysis, reducing the occurrence of gaps in the time series.

In order to achieve better results and improve the accuracy and stability of our analysis, it is important to consider all three performances. Based on the observations on 07 September and considering the mean value and standard deviation, we have determined that a maximum elevation angle of 32° and a time window length longer than 35 minutes yield more accurate and reliable results. Additionally, selecting a maximum elevation angle of 39° allows us to include more data points in the time series, further enhancing the quality of our analysis. These parameters can also be applied to future observations to ensure consistency and comparability in our results.

When using a rotated antenna, the quality of the signals improves, which allows for more accurate measurements. To determine the optimal parameters for the observation on 16

February, we examined the maximum elevation angle in the range of 30 to 60° and the time window length from 30 to 45 minutes. As there was no gauge data available for that day, we analyzed the standard deviation and point count, as shown in Figure 5.5a and Figure 5.5b. It is evident that the stability of the time series is significantly improved when using the rotated antenna. The standard deviation is below 4 cm for elevations higher than approximately 40°. To include more data in the analysis, we selected a maximum elevation angle of 60°, as signals with higher elevation may still be reflected by the water surface. The time window length does not have a significant impact on the results in this case, but for maximum point count, we chose a relatively short window of 30 minutes.

(a) standard deviation   *(b)* points counting
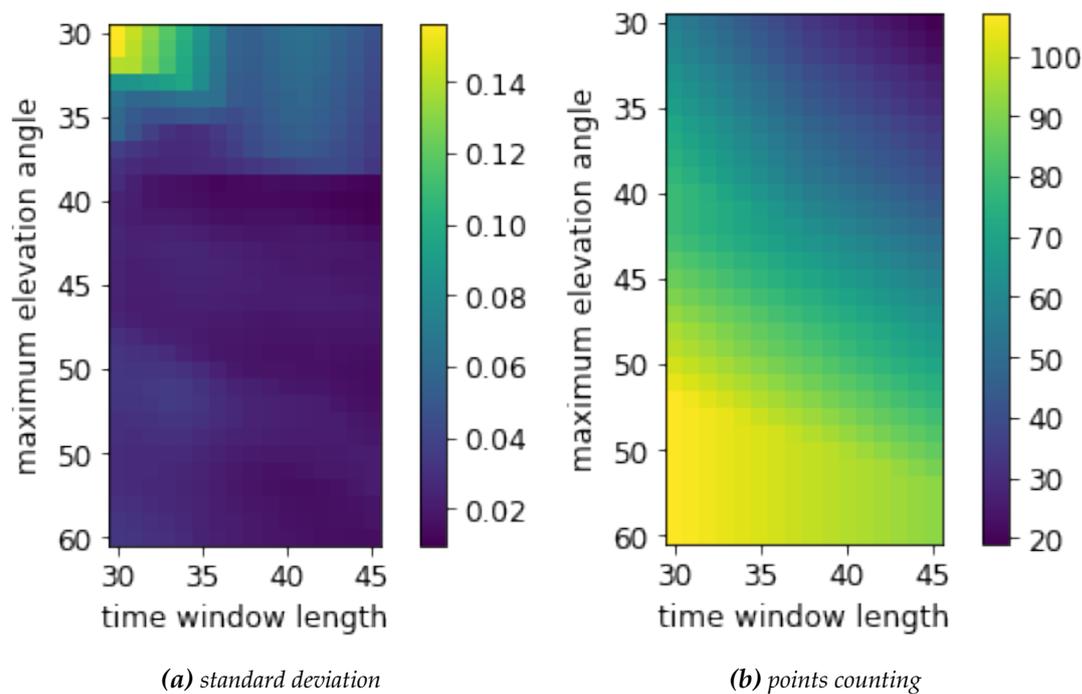
Figure 5.5: *Standard deviation and points counting using different maximum elevation angle and time window length for rotated receiver*

5.2 GNSS IR Result Quality

5.2.1 Time series from leveled Antennas

We initially leveled our receivers, similar to a standard GNSS observation for positioning purposes. The collected data were then processed using the method described in chapter 4, following the data filtering based on the determined windows. The resulting time series are depicted in Figure 5.6 to Figure 5.11. The stability and accuracy of the results could vary across the different campaigns, which can be attributed to the changing distribution of satellites each day. As we receive signals from different directions each time it passes the area, the variations in signal availability and noise levels can impact the accuracy of the results at certain time points. The mean height and standard deviation for each time series are summarized in Table 5.1.
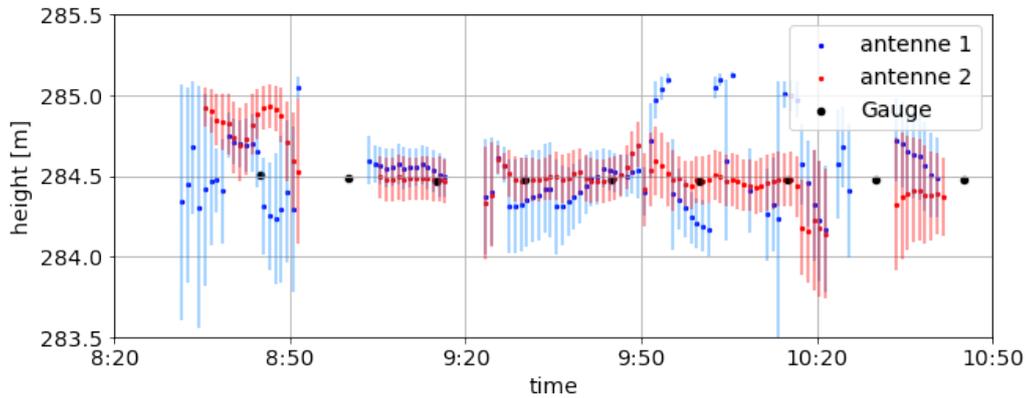
Figure 5.6: *Time series on 11 August 2022. Blue and red points are results from 2 antennes and the errors are plotted by errorbar. The black points are water level measured from gauge.*
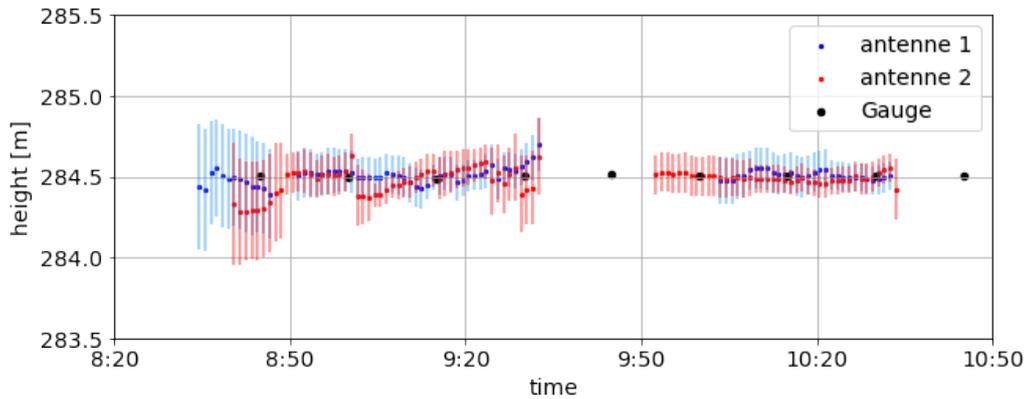
Figure 5.7: *Time series on 07 September 2022. Blue and red points are results from 2 antennes and the errors are plotted by errorbar. The black points are water level measured from gauge.*
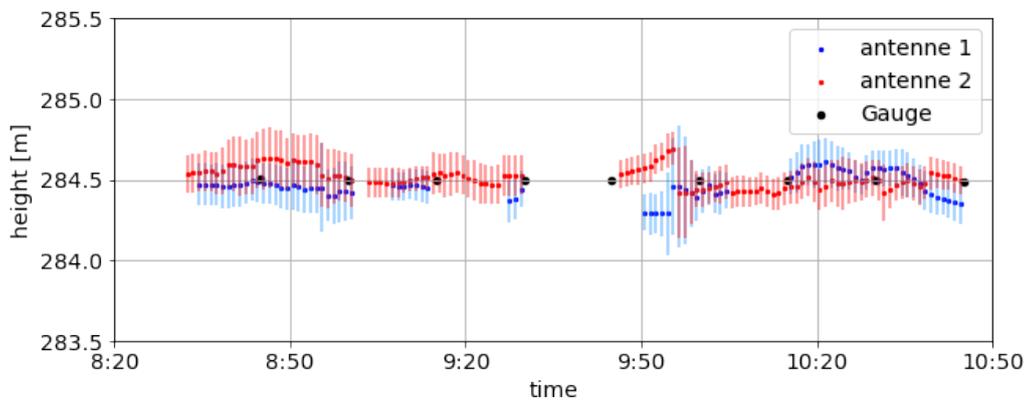
Figure 5.8: *Time series on 04 October 2022. Blue and red points are results from 2 antennes and the errors are plotted by errorbar. The black points are water level measured from gauge.*
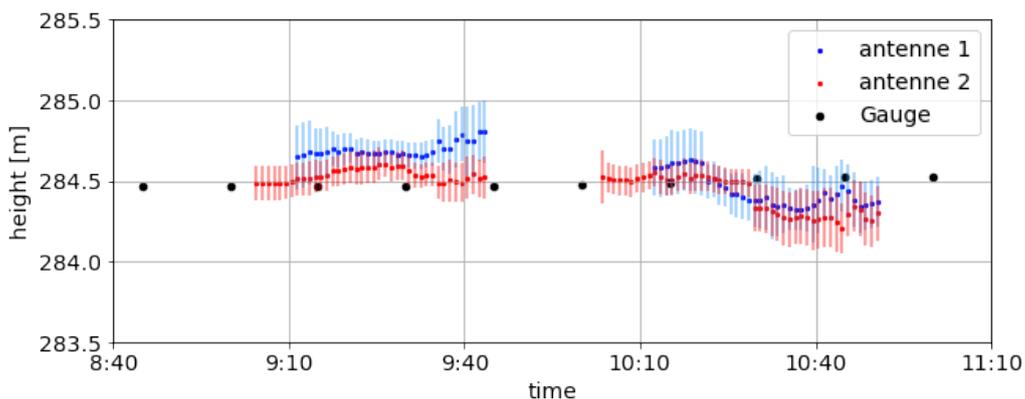
Figure 5.9: *Time series on 31 October 2022. Blue and red points are results from 2 antennes and the errors are plotted by errorbar. The black points are water level measured from gauge.*
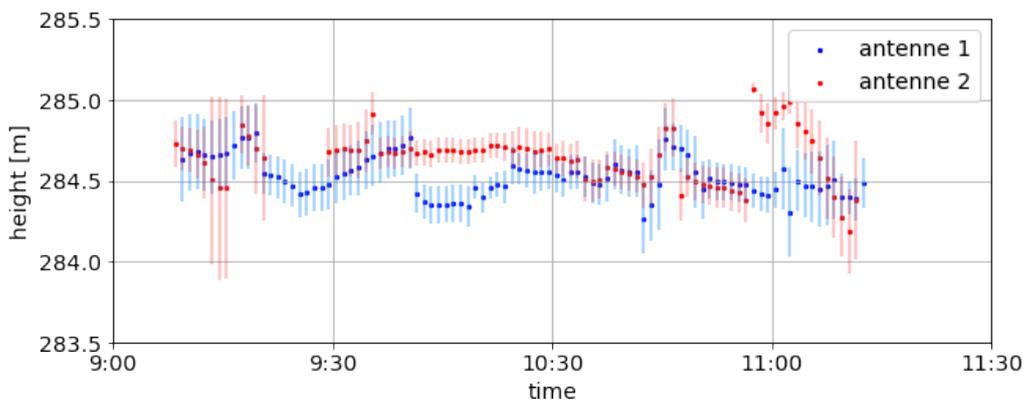
Figure 5.10: *Time series on 27 November 2022. Blue and orange points are results from 2 antennes. Blue and red points are results from 2 antennes and the errors are plotted by errorbar. From this campaign, the gauge data is not available anymore.*
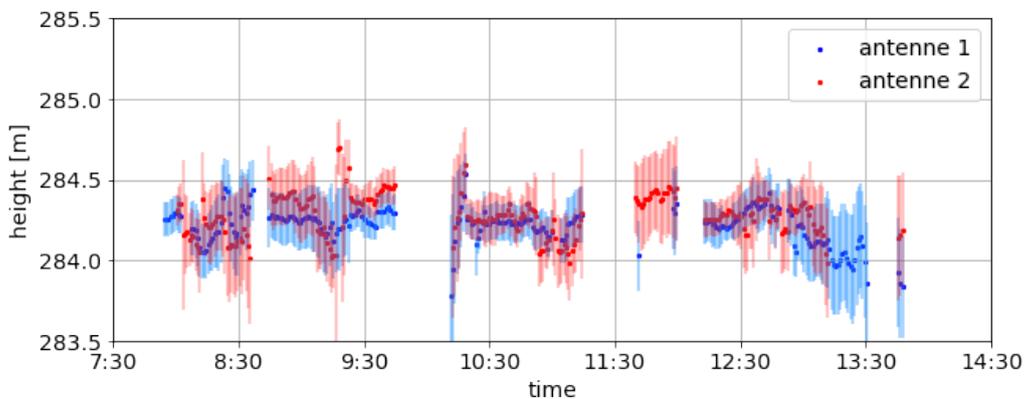
Figure 5.11: *Time series on 16 February 2023. Blue and orange points are results from 2 antennes.Blue and red points are results from 2 antennes and the errors are plotted by errorbar. The gauge data is not available.*

Date	receiver	gauge [m]	GNSS-IR mean [m]	GNSS-IR standard deviation [m]
11/08/22	1	284.483	284.52	0.22
	2		284.52	0.16
07/09/22	1	284.507	284.51	0.04
	2		284.48	0.07
04/10/22	1	284.499	284.46	0.08
	2		284.51	0.06
31/10/22	1	284.493	284.56	0.15
	2		284.46	0.11
27/11/22	1	nan	284.52	0.11
	2		284.64	0.16
16/02/23	1	nan	284.21	0.11
	3		284.27	0.13

Table 5.1: *mean value and standard deviation of the time series from Figure 5.6 to Figure 5.11, gauge mean is also provided when available at first 4 campaigns.*

During the period from August to November, the observation accuracy and stability varied, with some instances showing better results than others. However, the mean river surface height remained relatively stable at around 284.5 m. With the exception of receiver 1 in August, the standard deviation was below 20 cm for all three geodetic GNSS receivers. Given the challenging geometry of visible satellites in the Neckar river area, relying solely on the peak value from the multiplied LSP periodogram can still yield incorrect results. However, by considering consecutive points and taking the mean or median value of the time series, we can make a more accurate estimation of the water level height within a single measument campaign. This approach proves to be more reliable compared to direct LSP results in this particular context.

To validate our results, we compared the water levels based on gauge measurements with the corresponding time series from GNSS-IR, as shown in Figure 5.6 to Figure 5.9. We observed that the water levels remained relatively stable during each campaign, which aligns with our expectations. Furthermore, the water levels derived from GNSS-IR closely match the gauge measurements. In Table 5.1, we provide the mean water heights based on gauge data. The small differences of several centimeters between the mean heights(maximum 7 centimeters) obtained from GNSS-IR and the gauge measurements fall within the standard deviation of the time series.

5.2.2 Comparison of Time series from Leveled and Rotated Antennas

Despite our efforts to improve the data quality, the largest standard deviation of 20 cm is still relatively high compared to other methods based on gauge. However, when we attempted to rotate the antenna on February 16, 2023, for a duration of 2 hours, the resulting time series showed remarkable stability, as depicted in Figure 5.12. The standard deviation in this case was reduced to 2 cm, which is a significant improvement compared to the results obtained with the leveled antenna. To ensure that the improved stability was not solely due to exceptionally strong signals during the 2-hour period, we conducted another campaign using both a leveled antenna and a rotated antenna for comparison.
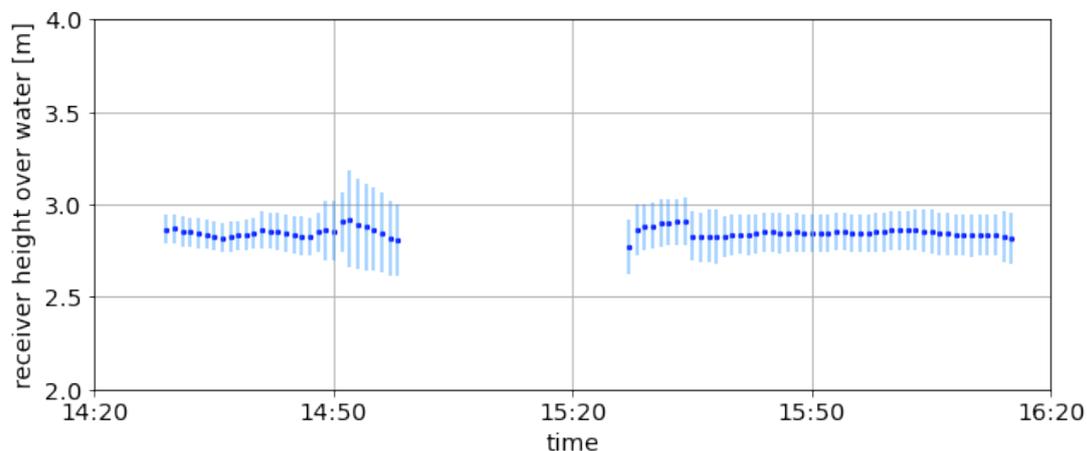
Figure 5.12: *Time series generated from data measured with rotated Leica GS15 antenna on 16 February 2023. Standard deviation is 3 cm*

On March 15, 2023, we conducted measurements using both a rotated antenna and a leveled antenna, allowing us to compare the results obtained from each setup. The time series generated from the rotated antenna, as shown in Figure 5.13, appears to be visually more stable than the time series from the leveled antenna. The results from leveled antenna also have higher uncertainty. It is worth noting that around 11:40, a ship passed through the measuring area, which is clearly visible in the time series generated from the rotated antenna. However, both time series exhibit two large gaps with no observations, which is due to the absence of visible satellites during those periods.
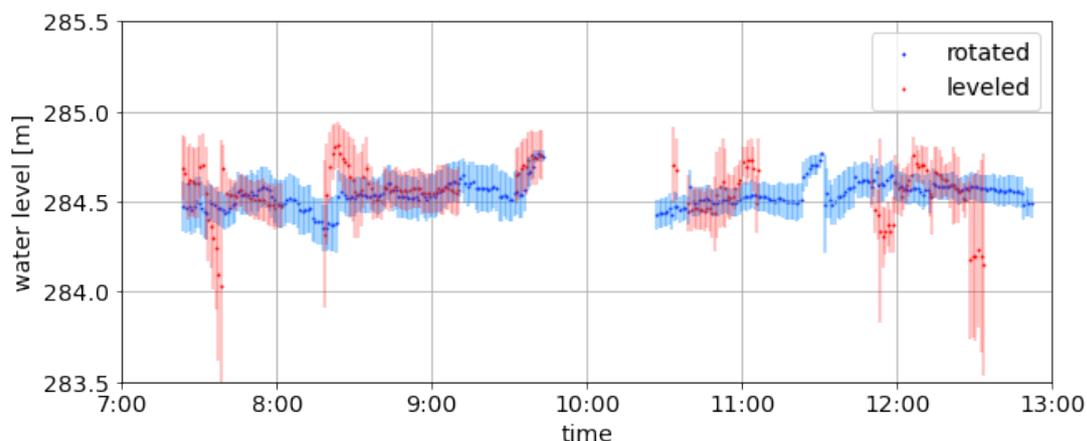
Figure 5.13: *Time series generated from data measured with rotated Leica GS15 antenna and leveled Leica GS25 on 16 February 2023. Blue points are for rotated antenna while orange one for leveled receiver*

In Table 5.2, we provide the mean height and standard deviation for the time series obtained from the rotated antenna and the leveled antenna. We observe that the time series from the rotated antenna has a significantly smaller standard deviation compared to the leveled antenna. However, the standard deviation is still higher compared to the results obtained on February 16. It is worth noting that there are some anomalies in the data. For example, around 11:40,

a ship passed through the river section. Additionally, there is an anomaly around 8:20, which may be attributed to poor satellite geometry during that time.

	mean height [m]	standard deviation [m]
leveled antenna	284.58	0.15
rotated antenna	284.58	0.06

Table 5.2: *mean height and standard deviation of the 2 time series demonstrated in Figure 5.13*

5.2.3 Comparison of GNSS-IR and Sentinel-3A

In Figure 5.14 to Figure 5.20, we present the satellite altimetry results for the Neckar River. It is evident that using satellite altimetry for a narrow river like the Neckar poses significant challenges. On February 16, no valid signals were received, indicating the difficulty in obtaining accurate measurements in such environments. On September 7, none of the retrackers produced results that closely matched the mean water level from gauge. This may be due to the inability of the software to find valid waveforms or the tracking of signals that are similar but not actually from the water surface. In Figure 5.15 and Figure 5.18, the OCEP and ICES retrackers did not yield satisfactory results on the returned signals. However, the other five retrackers (Ocean(SAR), OCOG(SAR), Ice(LRM), Ice-sheet(LRM), and Sea-Ice(SAR)) demonstrated better performance. For example, the ISS retracker accurately determined water levels on October 31 and November 11. However, it should be noted that these retrackers still exhibit some errors and variability in their water level estimations. Overall, the satellite altimetry results show the challenges associated with accurately measuring water levels in a narrow river like the Neckar. The performance of different retrackers varies, and careful analysis and consideration are required when interpreting the results.
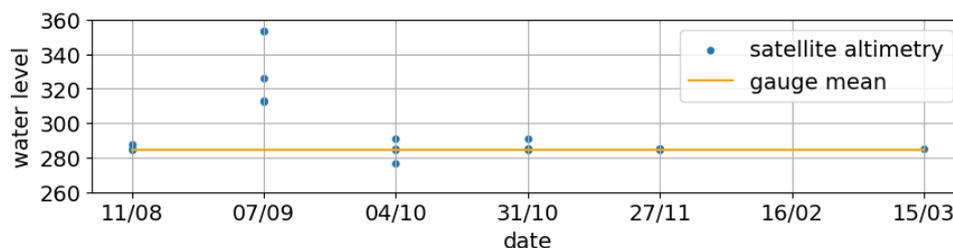
Figure 5.14: *Ellisoidal water level from satellite altimetry with ocean retracker of SAR mode in WGS84 frame. The blue points are the water level measured from Sentinel-3A and yellow line is for mean value from the available gauge data.*
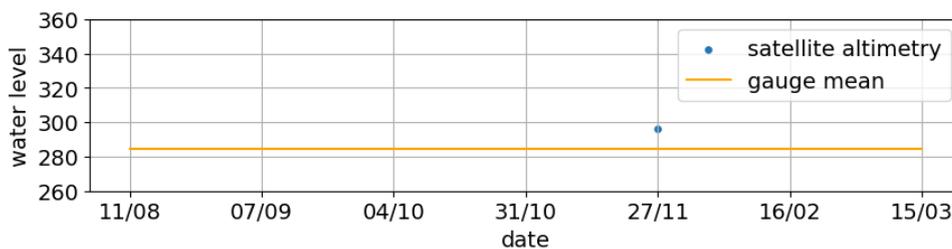
Figure 5.15: *Ellisoidal water level from satellite altimetry with ocean retracker of LRM mode in WGS84 frame. The blue points are the water level measured from Sentinel-3A and yellow line is for mean value from the available gauge data. The only result from this retracker is too far away from the water level measured from gauge.*
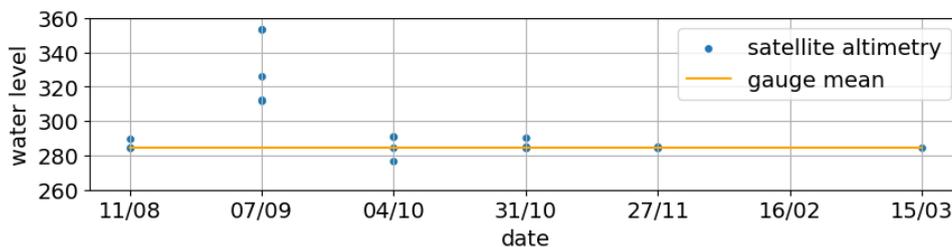
Figure 5.16: *Ellisoidal water level from satellite altimetry with OCOG of SAR mode in WGS84 frame. The blue points are the water level measured from Sentinel-3A and yellow line is for mean value from the available gauge data.*
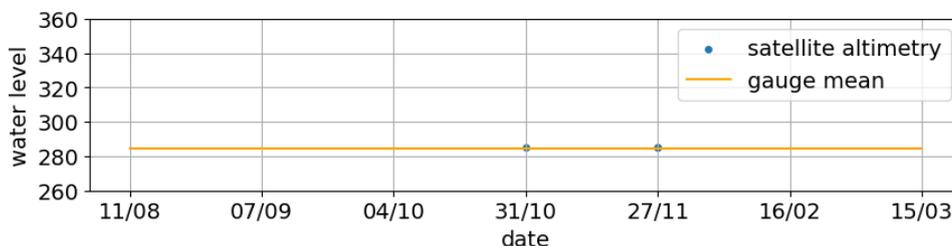
Figure 5.17: *Ellisoidal water level from satellite altimetry with ice retracker of LRM mode in WGS84 frame. The blue points are the water level measured from Sentinel-3A and yellow line is for mean value from the available gauge data.*
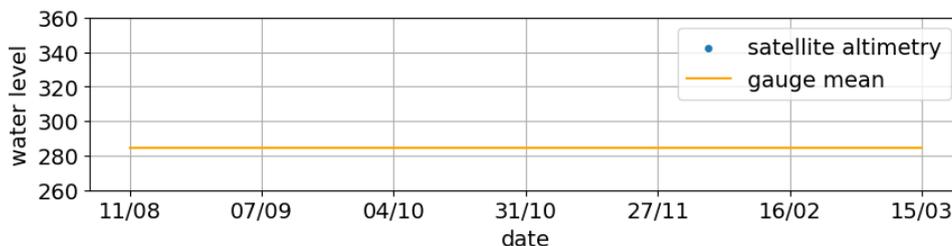
Figure 5.18: *Ellisoidal water level from satellite altimetry with ice sheet retracker of SAR mode in WGS84 frame. Yellow line is for mean value from the available gauge data. There is no data from satellite on this day for this area.*
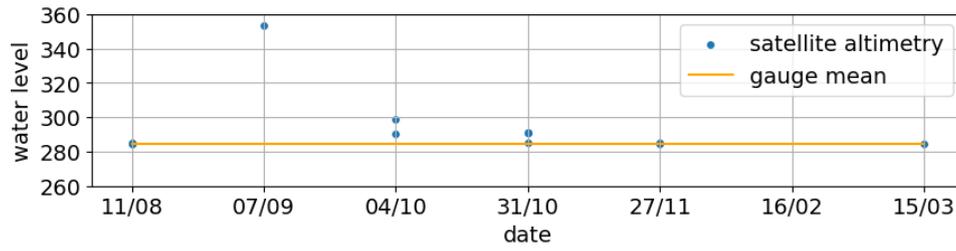
Figure 5.19: *Ellisoidal water level from satellite altimetry with ice-sheet retracker of LRM mode in WGS84 frame. The blue points are the water level measured from Sentinel-3A and yellow line is for mean value from the available gauge data.*
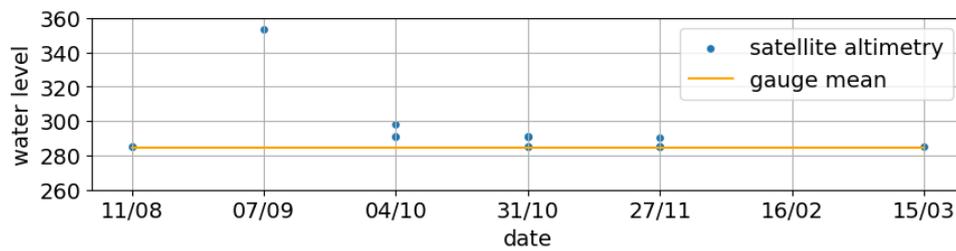
Figure 5.20: *Ellisoidal water level from satellite altimetry with sea ice retracker of SAR mode in WGS84 frame. The blue points are the water level measured from Sentinel-3A and yellow line is for mean value from the available gauge data.*

To validate the satellite altimetry results, we compared them to the mean height obtained from both receivers during the entire measurement campaign. If the satellite altimetry result fell within the range of ± 3 standard deviations (σ) of the mean height, it was considered a valid result. This approach helps to assess the agreement between the satellite altimetry measurements and the GNSS-IR measurements from the receivers. By applying this validation criterion, we can identify which satellite altimetry results are consistent with the GNSS-IR measurements and fall within an acceptable range of variability. This allows us to evaluate the accuracy and reliability of the satellite altimetry data in relation to the GNSS-IR measurements.

$$\bar{h}_{\text{GNSS IR}} - 3\sigma_{\text{GNSS IR}} < h_{\text{valid altimetry}} < \bar{h}_{\text{GNSS IR}} + 3\sigma_{\text{GNSS IR}} \qquad (5.1)$$

Using the criterion above we can exclude 2 retrackers which don't provide valid results. In order to assess the performance of rest retrackers, we have compiled the number of valid water level results and the mean values obtained from each retracker in Table 5.3 and Table 5.4 respectively. These numbers are demonstrated in Figure 5.21 graphiclly together with gauge value and GNSS-IR results. In Table 5.5 we present the difference between the GNSS-IR mean and satellite altimetry mean. They provide an overview of the performance of each retracker in terms of the quantity and accuracy of the water level measurements. From Table 5.3 we see that the OCOG retrackers has the most consistant performance since it returns the valid results, no matter other retrackers computes valid water levels or not. When all retrackers are able to give the valid numbers in one measurement, OCOG has the most result. Figure 5.21 and Table 5.4 shows the mean of each retracker at every single measurement and accuracy of these retrackers. The water levels from altimetry are higher than from GNSS-IR for all retrackers in every campaign. This offset is in the order of several decimeters for most retrackers. In

Table 5.5 it can be seen that OCOG of SAR nad Ice-sheet of LRM are more close to the water level measured from GNSS-IR, the OCOG is from 0.03 to 0.17 meter higher than GNSS-IR result and Ice-sheet from 0.07 to 0.24 while the other retrackers are more than 20 centimeter higher, also indicating the existance of this offset, though it is unclear whether it is a general characteristic or specific to the Neckar environment because the offset from each retracker is also different from about 0.1 to 0.4 meters.

The better performance of the OCOG retracker suggests that there is room for improvement in the algorithms used by the other retrackers. These findings highlight the potential for further refining the retracking algorithms to enhance the accuracy and reliability of satellite altimetry measurements, particularly in challenging environments such as the Neckar River.

	Ocean of SAR	OCOG of SAR	Ice of LRM	Ice-sheet of LRM	Sea ice of SAR
11/08	2/3	2/3	0/3	3/3	2/3
07/09	0/5	0/5	0/5	0/5	0/5
04/10	0/4	1/4	0/4	0/4	0/4
31/10	2/5	3/5	0/5	0/5	1/5
27/11	3/4	4/4	2/4	2/4	2/4
16/02	0/0	0/0	0/0	0/0	0/0
15/03	1/1	1/1	0/1	1/1	1/1

Table 5.3: valid result number of 5 retrackers

	Ocean of SAR	OCOG of SAR	Ice of LRM	Ice-sheet of LRM	Sea ice of SAR
11/08	284.80	284.60	nan	284.70	284.88
07/09	nan	nan	nan	nan	nan
04/10	nan	284.64	nan	nan	nan
31/10	284.83	284.71	nan	nan	284.94
27/11	284.85	284.75	284.94	284.65	284.99
16/02	nan	nan	nan	nan	nan
15/03	284.83	284.64	nan	284.75	284.94

Table 5.4: mean of the valid result of 5 retrackers [m]

Date	Ocean of SAR	OCOG of SAR	Ice of LRM	Ice-sheet of LRM	Sea ice of SAR
11/08	0.23	0.03	nan	0.13	0.31
07/09	nan	nan	nan	nan	nan
04/10	nan	0.17	nan	nan	nan
31/10	0.29	0.17	nan	nan	0.40
27/11	0.27	0.17	0.36	0.07	0.41
16/02	nan	nan	nan	nan	nan
15/03	0.32	0.13	nan	0.24	0.43

Table 5.5: Difference between the satellite altimetry and GNSS-IR[m]
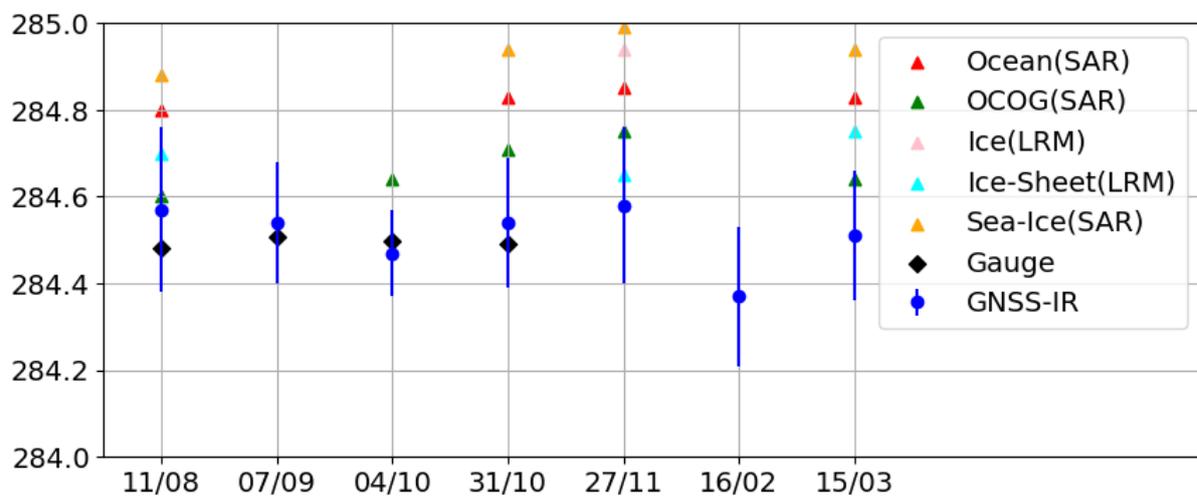
Figure 5.21: *Overview of the performance of each retracker, the blue points with errorbar state the mean of each measurements with one standard deviation range, and black points are the available gauge value.*

Chapter 6

Conclusion and Outlook

6.1 Conclusion

6.1.1 Measurement Summary

Due to the challenging environment of the Neckar River, we have made several adjustments to our measurement location and principles in order to obtain more accurate results. We would also like to summarize our experiences to benefit future GNSS-IR research and studies.

The main objective is to receive as many valid signals as possible. When selecting our measurement location, we must consider how we can increase the valid azimuth and elevation range, especially for smaller bodies of water like the Neckar River. Ideally, the receiver would be positioned in the center of the water body to capture signals from all visible satellites, but in reality, we need to find a location with a clear view of the water. For larger bodies of water, such as the GNSS-IR station at Friday Harbor, we can aim for a location where signals can be received in an azimuth range of approximately 270 degrees, or even set up the station on a straight lakeshore, riverbank, or seashore to capture signals from half of the sky. For smaller rivers, we must be more cautious, as simply placing antennas along the riverside may not capture reflected signals at low elevation angles, which are crucial in GNSS-IR studies. The best approach is to locate an island in the water, where we are allowed to take measurements at the center of the water body. Similarly, we should avoid bend sections of rivers for the same reason.

Another option is to mount the GNSS antenna on a bridge, but this may not be feasible for narrow rivers. The higher position of the antenna means that the reflected signal points are further away, which could affect the analysis later on: in order to use the signals reflected by the water surface in our analysis, we must choose a smaller azimuth range than data collected by an antenna at the same location but with a lower height. Although signals from high elevation angles may not be as useful as those from low elevation angles, we still include them in our final analysis. To achieve this, the antenna should be placed as close to the water as possible.

Some studies have used low-cost GNSS antennas to obtain better SNR data. While we have not tested this possibility, we have demonstrated that even with a geodetic GNSS antenna, it is possible to obtain excellent data by rotating the antenna. There are no strict rules on how many degrees the antenna should be rotated, as several factors must be considered:

- We need to ensure that the side of the antenna that receives the signal is oriented towards the water.

- Supporting measurements are necessary to determine the absolute height of the antenna phase center. Another GNSS antenna can be helpful, or the rotated antenna can be placed near a height reference if possible.

In addition, it's important to avoid river sections that are crowded with boats or other objects. In environments with many trees or tall buildings, it can be difficult to determine the source of the reflected signals, so it's best to steer clear of these areas.

When beginning the measurements, there are several things to double-check.

- Some antennas filter out signals with low elevation angles, so it's important to ensure that this setting is deactivated.

- Use higher sample rate.

- Make sure to allow the antenna to track all possible signals.

- If you choose to maintain a normal position instead of rotating the receiver, it is important to document the offset between the positioning point and the phase center, note that this offset can vary for different signals.

- If possible, document the time when large objects such as boats pass by, as this can make the analysis much easier later on.

Another important factor that cannot be neglected, although unrelated to the quality of the measurements, is power. The length of time that the power lasts directly affects how much data we can collect during a single campaign.

6.1.2 Conclusion of Results

Based on the findings presented in the previous chapters, it is evident that GNSS-IR can serve as a reliable method for measuring water levels, even in challenging environments. The technique has demonstrated its capability to validate satellite altimetry measurements, such as those provided by the Sentinel-3 mission. With appropriate equipment and suitable measurement locations, GNSS-IR can achieve sub cecimeter-level accuracy, even in complex and dynamic environments.

GNSS-IR offers several advantages, including its versatility and potential as a replacement for traditional methods such as satellite altimetry and gauges. In cases where satellite altimetry may face limitations or fail to provide accurate measurements, GNSS-IR can offer a robust alternative. Additionally, GNSS-IR can overcome the challenges associated with building and maintaining gauging stations in remote or inaccessible areas.

The altimetry results from the Sentinel-3 mission were found to be generally close to GNSS-IR results. The difference between the best OCOG retracker and GNSS-IR is lower than 0.2 meters and sometimes even 0.03 meters with good waveforms. The Ice-sheet of LRM is the second good retrackers in this case. It is important to carefully select the retracker algorithm to ensure accurate results, especially for small water bodies. In the study, the OCOG

retracker was determined to be the most suitable for the Neckar River in the Stuttgart area. GNSS-IR can be trusted to measure the water level and therefore be used to validate the satellite altimetry based on accuracy and flexibility. Nevertheless, it is worth noting that an offset correction is still required to achieve optimal accuracy for satellite altimetry according to our study. This offset is different for different retrackers and the reason of this offset needs further investigation.

Overall, the combination of GNSS-IR and satellite altimetry provides a comprehensive and reliable approach for water level monitoring and validation. By leveraging the strengths of both techniques, researchers and water resource managers can gain valuable insights into water dynamics and improve our understanding of hydrological processes in various environments.

6.2 Outlook

There are indeed several areas for improvement in this work, and further research and exploration can contribute to enhancing the methodology and results. Here are some potential avenues for improvement:

- Relationship between azimuth and elevation range: Finding the optimal relationship between azimuth and elevation range filters can be a valuable step. Exploring different configurations and conducting thorough analyses can help define the best approach for assigning azimuth ranges based on elevation angles.

- Accuracy assessment: Developing a robust and reliable method for assessing the accuracy of the results is crucial. Exploring different approaches, such as comparing the results with ground truth data or using statistical measures, can provide a more comprehensive understanding of the accuracy and reliability of the GNSS-IR measurements.

- Inclusion of other navigation systems: Expanding the analysis to include signals from other navigation systems, such as Beidou, can increase the number of available signals and improve the accuracy and reliability of the GNSS-IR measurements. Investigating the compatibility and performance of these additional signals can enhance the overall capability of the method.

- Evaluation of low-cost GNSS receivers: Comparing the performance of low-cost GNSS receivers with traditional geodetic equipment can provide valuable insights into their suitability for GNSS-IR measurements. This evaluation can help determine the feasibility and cost-effectiveness of using low-cost receivers in future studies.

By addressing these areas for improvement, the GNSS-IR methodology can be further refined and enhanced, leading to more accurate and reliable measurements of environmental parameters and facilitating their comparison with other measurement techniques.

Finally, the retracking algorithm for satellite altimetry, such as Sentinel-3A, is an area that can benefit from further improvements. Despite the advancements made in retracking techniques, there are still challenges and limitations that need to be addressed.

List of Figures

List of Tables

Bibliography

Ashraf, M. A. and Mohd Hanafiah, M. (2019), 'Sustaining life on earth system through clean air, pure water, and fertile soil'.
URL: *https://doi.org/10.1007/s11356-018-3528-3*

Bilich, A. and Larson, K. M. (2007), 'Correction published 29 march 2008: Mapping the GPS multipath environment using the signal-to-noise ratio (SNR)', *Radio Science* **42**(06), 1–16.
URL: *https://doi.org/10.1029/2007RS003652*

Bosseler, B., Salomon, M., Schlüter, M. and Rubinato, M. (2021), 'Living with urban flooding: A continuous learning process for local municipalities and lessons learnt from the 2021 events in germany', *Water* **13**(19), 2769.
URL: *https://doi.org/10.3390/w13192769*

Braasch, M. (1996), Gps multipath model validation, *in* 'Proceedings of Position, Location and Navigation Symposium - PLANS '96', pp. 672–678.
URL: *https://doi.org/10.1109/PLANS.1996.509144*

Davie, T. (2019), *Fundamentals of hydrology*, Routledge.

Davis, C. H. (1993), 'A surface and volume scattering retracking algorithm for ice sheet satellite altimetry', *IEEE transactions on geoscience and remote sensing* **31**(4), 811–818.
URL: *https://doi.org/10.1109/36.239903*

Deng, X. and Featherstone, W. (2006), 'A coastal retracking system for satellite radar altimeter waveforms: Application to ERS-2 around australia', *Journal of Geophysical Research: Oceans* **111**(C6).
URL: *https://doi.org/10.1029/2005JC003039*

Estey, L. H. and Meertens, C. M. (1999), 'TEQC: the multi-purpose toolkit for GPS/GLONASS data', *GPS solutions* **3**(1), 42–49.
URL: *https://doi.org/10.1007/PL00012778*

Geng, J., Chen, X., Pan, Y., Mao, S., Li, C., Zhou, J. and Zhang, K. (2019), 'PRIDE PPP-AR: an open-source software for GPS PPP ambiguity resolution', *GPS Solutions* **23**, 1–10.
URL: *https://doi.org/10.1007/s10291-019-0888-1*

Gleick, P. H. (2003), 'Global freshwater resources: soft-path solutions for the 21st century', *Science* **302**(5650), 1524–1528.
URL: *https://doi.org/10.1126/science.1089967*

Goudie, A. S. (2006), 'Global warming and fluvial geomorphology', *Geomorphology* **79**(3-4), 384–394.
URL: *https://doi.org/10.1016/j.geomorph.2006.06.023*

Group, A. H., Vörösmarty, C., Askew, A., Grabs, W., Barry, R., Birkett, C., Döll, P., Goodison, B., Hall, A., Jenne, R. et al. (2001), 'Global water data: A newly endangered species', *Eos, Transactions American Geophysical Union* **82**(5), 54–58.
URL: *https://doi.org/10.1029/01EO00031*

Katzberg, S. J., Torres, O., Grant, M. S. and Masters, D. (2006), 'Utilizing calibrated GPS reflected signals to estimate soil reflectivity and dielectric constant: Results from SMEX02', *Remote sensing of environment* **100**(1), 17–28.
URL: *https://doi.org/10.1016/j.rse.2005.09.015*

Larson, K. M. and Nievinski, F. G. (2013), 'GPS snow sensing: results from the earthscope plate boundary observatory', *GPS solutions* **17**, 41–52.
URL: *https://doi.org/10.1007/s10291-012-0259-7*

Larson, K. M., Ray, R. D. and Williams, S. D. (2017), 'A 10-year comparison of water levels measured with a geodetic gps receiver versus a conventional tide gauge', *Journal of Atmospheric and Oceanic Technology* **34**(2), 295–307.

Lomb, N. R. (1976), 'Least-squares frequency analysis of unequally spaced data', *Astrophysics and space science* **39**, 447–462.
URL: *https://doi.org/10.1007/BF00648343*

Lorenz, C., Kunstmann, H., Devaraju, B., Tourian, M. J., Sneeuw, N. and Riegger, J. (2014), 'Large-scale runoff from landmasses: a global assessment of the closure of the hydrological and atmospheric water balances', *Journal of Hydrometeorology* **15**(6), 2111–2139.
URL: *https://doi.org/10.1175/JHM-D-13-0157.1*

Lutz, A., Immerzeel, W., Shrestha, A. B. and Bierkens, M. (2014), 'Consistent increase in high asia's runoff due to increasing glacier melt and precipitation', *Nature Climate Change* **4**(7), 587–592.
URL: *https://doi.org/10.1038/nclimate2237*

Martin, T. V., Zwally, H. J., Brenner, A. C. and Bindschadler, R. A. (1983), 'Analysis and retracking of continental ice sheet radar altimeter waveforms', *Journal of Geophysical Research: Oceans* **88**(C3), 1608–1616.
URL: *https://doi.org/10.1029/JC088iC03p01608*

Park, K.-D., Elósegui, P., Davis, J., Jarlemark, P., Corey, B., Niell, A., Normandeau, J., Meertens, C. and Andreatta, V. (2004), 'Development of an antenna and multipath calibration system for global positioning system sites', *Radio Science* **39**(5), 1–13.
URL: *https://doi.org/10.1029/2003RS002999*

Pekel, J.-F., Cottam, A., Gorelick, N. and Belward, A. S. (2016), 'High-resolution mapping of global surface water and its long-term changes', *Nature* **540**(7633), 418–422.
URL: *https://doi.org/10.1038/nature20584*

Purnell, D. J., Gomez, N., Minarik, W., Porter, D. and Langston, G. (2021), 'Precise water level measurements using low-cost GNSS antenna arrays', *Earth Surface Dynamics* **9**(3), 673–685.
URL: *https://doi.org/10.5194/esurf-9-673-2021*

Rao, B. R., McDonald, K. and Kunysz, W. (2013), *GPS/GNSS Antennas*, Artech House.
URL: *https://doi.org/10.3390/rs5020808*

Ridley, J. and Partington, K. (1988), 'A model of satellite radar altimeter return from ice sheets', *Remote Sensing* **9**(4), 601–624.
 URL: *https://doi.org/10.1080/01431168808954881*

Robinson, I. S. (2004), *Measuring the oceans from space: the principles and methods of satellite oceanography*, Springer Science & Business Media.

Roesler, C. and Larson, K. M. (2018), 'Software tools for GNSS interferometric reflectometry (GNSS-IR)', *GPS solutions* **22**(3), 80.
 URL: *https://doi.org/10.1007/s10291-018-0744-8*

Santamaría-Gómez, A. and Watson, C. (2017), 'Remote leveling of tide gauges using gnss reflectometry: case study at spring bay, australia', *GPS solutions* **21**, 451–459.
 URL: *https://doi.org/10.1007/s10291-016-0537-x*

Scargle, J. D. (1982), 'Studies in astronomical time series analysis. ii-statistical aspects of spectral analysis of unevenly spaced data', *Astrophysical Journal, Part 1, vol. 263, Dec. 15, 1982, p. 835-853.* **263**, 835–853.
 URL: *http://dx.doi.org/10.1086/160554*

Shu, S., Liu, H., Beck, R. A., Frappart, F., Korhonen, J., Xu, M., Yang, B., Hinkel, K. M., Huang, Y. and Yu, B. (2020), 'Analysis of sentinel-3 sar altimetry waveform retracking algorithms for deriving temporally consistent water levels over ice-covered lakes', *Remote Sensing of Environment* **239**, 111643.
 URL: *https://doi.org/10.1016/j.rse.2020.111643*

Song, M., He, X., Wang, X., Zhou, Y. and Xu, X. (2019), 'Study on the quality control for periodogram in the determination of water level using the gnss-ir technique', *Sensors* **19**(20).
 URL: *https://doi.org/10.3390/s19204524s*

Strandberg, J., Hobiger, T. and Haas, R. (2016), 'Improving GNSS-R sea level determination through inverse modeling of snr data', *Radio Science* **51**(8), 1286–1296.
 URL: *https://doi.org/10.1002/2016RS006057*

Tourian, M. J. (2013), *Application of spaceborne geodetic sensors for hydrology*.
 URL: *http://dx.doi.org/10.13140/2.1.3194.3043*

VanderPlas, J. T. (2018), 'Understanding the Lomb-Scargle Periodogram', *The Astrophysical Journal Supplement Series* **236**(1), 16.
 URL: *https://dx.doi.org/10.3847/1538-4365/aab766*

Wada, Y., Van Beek, L. and Bierkens, M. F. (2011), 'Modelling global water stress of the recent past: on the relative importance of trends in water demand and climate variability', *Hydrology and Earth System Sciences* **15**(12), 3785–3808.
 URL: *https://doi.org/10.5194/hess-15-3785-2011*

Wang, X., Zhang, Q. and Zhang, S. (2019), 'Sea level estimation from snr data of geodetic receivers using wavelet analysis', *GPS solutions* **23**, 1–14.
 URL: *https://doi.org/10.1007/s10291-018-0798-7*

Wingham, D., Rapley, C. and Griffiths, H. (1986), New techniques in satellite altimeter tracking systems, *in* 'Proceedings of IGARSS', Vol. 86, pp. 1339–1344.

Zimmermann, F., Schmitz, B., Klingbeil, L. and Kuhlmann, H. (2019), 'Gps multipath analysis using fresnel zones', *Sensors* **19**(1).
    URL: *https://www.mdpi.com/1424-8220/19/1/25*

Appendix A

Transformation

The coordinates from PRIDE are in ellipsoidal coordinate system WGS84 (x, y and z) and need to be transformed in geodetic longitude λ, latitude φ and height h. We present this process below: The longitude λ can be simply calculated by:

$$\lambda = \arctan\left(\frac{y}{x}\right) \tag{A.1}$$

The latitude φ and height h, however have to be calculated with iteration. We first calculate 2 start values:

$$p_0 = \sqrt{x^2 + y^2} \tag{A.2}$$

$$\varphi_0 = \arctan\left(\frac{z}{p_0} \cdot \left(1 - e^2\right)^{-1}\right) \tag{A.3}$$

After that, we do the following calculation literately, until $d\varphi$ is smaller than the threshold:

$$l = \sqrt{a^2 \cdot \cos^2\left(\varphi_0\right) + b^2 \cdot \sin^2\left(\varphi_0\right)} \tag{A.4}$$

$$N = \frac{a^2}{l} \tag{A.5}$$

$$h = \frac{p_0}{\cos\left(\varphi_0\right)} - N \tag{A.6}$$

$$\varphi = \arctan\left(\frac{z}{p_0} \cdot \left(1 - e^2 \cdot \left(\frac{N}{N+h}\right)\right)^{-1}\right) \tag{A.7}$$

$$d\varphi = |\varphi - \varphi_0| \tag{A.8}$$

$$\varphi_0 = \varphi \tag{A.9}$$

where a, b and e are semi-major axis, semi-minor axis and eccentricity of the reference ellipsoid.

Appendix B

First Fresnel Zone

We start with λ for wavelength, h for antenna height over reflection surface, and ε and α for satellite elevation angle and azimuth, then the first Fresnel Zone dimensions are:

$$d = \frac{\lambda}{2} \tag{B.1}$$

$$R = \frac{h}{\tan \varepsilon} + \frac{\frac{d}{\sin \varepsilon}}{\tan \varepsilon} \tag{B.2}$$

$$b = 2 \cdot d \cdot \frac{h}{\sin \varepsilon} + \sqrt{\frac{d}{\sin^2 \varepsilon}} \tag{B.3}$$

$$a = \frac{b}{\sin \varepsilon} \tag{B.4}$$

Where a and b are semi-major and semi-minor axis of the ellipse. Its perimeter can be discretized as function of the inner angle $\vartheta \in [0, 2\pi]$

$$x' = a \cos \vartheta + R \tag{B.5}$$

$$y' = b \sin \vartheta \tag{B.6}$$

And the semi-major axis is finally aligned with the satellite azimuth in local coordinate system:

$$x = \sin(\alpha) x' - \cos(\alpha) y' \tag{B.7}$$

$$y = \sin(\alpha) y' + \cos(\alpha) x' \tag{B.8}$$

Appendix C

TEQC

C.1 Translation

The data binary format from Leica antenna is mdb, thus the command for the translation is:

```
teqc.exe −lei mdb −st yyyy_mm_dd :HH:MM: SS −e yyyy_mm_dd :HH:MM: SS
+obs xxxxxxxx.22o +nav xxxxxxxx.22n,xxxxxxxx.22g,xxxxxxxx.22d,
xxxxxxxx.22l +C2 +L5 +L6 +L7 +L8 binaryfile.m00
```

The option "-lei mdb" in the command refers to the Leica mdb format. The time specified after "-st" and "-e" represents the approximate start and end times of the measurement. The options "+obs" and "+nav" indicate the generated RINEX observation file and ephemeris file names, respectively. The additional options "+C2", "+L5", "+L6", "+L7", and "+L8" are used to extract the associated data, such as the L8 signal for Galileo E5. These options allow for the selective extraction of specific data types from the input files during the conversion process.

C.2 Elevation, Azimuth and SNR Extracting

After generating the RINEX file using Teqc, the software offers a quality check function that allows us to calculate the elevation and azimuth angles, as well as extract the signal-to-noise ratio (SNR) data.

```
teqc.exe +qc +plot −nav xxxxxxxx.22n, xxxxxxxx.22g,
xxxxxxxx.22l xxxxxxxx.22o > xxxxxxxx.qc
```

The provided command above allows for quality checking using Teqc. After inputting the RINEX files (observation and ephemeris), a quality report file will be generated, documenting the quality assessment of the RINEX data. By adding the argument "+plot" to the command, Teqc will generate additional files known as "compact files" with extensions such as ele, azi, sn1, sn2, sn5, etc. These compact files contain the recorded elevation, azimuth, and corresponding SNR data.